

THE RADIUS–LUMINOSITY RELATIONSHIP FOR ACTIVE GALACTIC NUCLEI: THE EFFECT OF HOST-GALAXY STARLIGHT ON LUMINOSITY MEASUREMENTS II. THE FULL SAMPLE OF REVERBERATION-MAPPED AGNS

MISTY C. BENTZ^{1,2}, BRADLEY M. PETERSON^{2,3}, HAGAI NETZER⁴, RICHARD W. POGGE^{2,3}, MARIANNE VESTERGAARD⁵

(Received: Accepted)
Draft version October 23, 2018

ABSTRACT

We present high-resolution *HST* images of all 35 AGNs with optical reverberation-mapping results, which we have modeled to create a nucleus-free image of each AGN host galaxy. From the nucleus-free images, we determine the host-galaxy contribution to ground-based spectroscopic luminosity measurements at $\lambda 5100 \text{ \AA}$. After correcting the luminosities of the AGNs for the contribution from starlight, we re-examine the $H\beta$ $R_{\text{BLR}}-L$ relationship. Our best fit for the relationship gives a powerlaw slope of 0.52 with a range of 0.45–0.59 allowed by the uncertainties. This is consistent with our previous findings, and thus still consistent with the naive assumption that all AGNs are simply luminosity-scaled versions of each other. We discuss various consistency checks relating to the galaxy modeling and starlight contributions, as well as possible systematic errors in the current set of reverberation measurements from which we determine the form of the $R_{\text{BLR}}-L$ relationship.

Subject headings: galaxies: active — galaxies: nuclei — galaxies: photometry — galaxies: Seyfert

1. INTRODUCTION

One of the key developments in extragalactic astronomy over the past decade has been the discovery that supermassive black holes are present in most, if not all, galaxies having a stellar bulge. Remarkably, the mass of the black hole is tightly correlated with the stellar velocity dispersion of the host galaxy bulge (Ferrarese & Merritt 2000; Gebhardt et al. 2000), pointing to a close link between the growth and evolution of galaxy stellar populations and the growth of nuclear black holes. Determining the masses of black holes in active galaxies is a crucial step toward understanding this connection, and provides fundamental insight into the physics of accretion and emission processes in the black hole environment.

Unfortunately, most active galactic nuclei (AGNs) are too distant for black hole masses to be measured using spatially resolved stellar or gas dynamics. The technique that has been most successful for the measurement of the black hole mass (M_{BH}) in AGNs is reverberation mapping (Blandford & McKee 1982; Peterson 1993). With this technique, the AGN continuum (typically measured at 5100 \AA) and broad emission lines (most notably, $H\beta$) are monitored over an extended time period. Since the emission-line regions are photoionized by the central source, changes in the AGN continuum strength are followed by changes in the emission-line fluxes, with a time lag that depends on the light-travel time across the broad-line region (BLR). This time lag can be measured by cross-correlation of the continuum and emission-line light curves, and gives the radius of the BLR. Combining the BLR radius with the broad

emission-line velocity width then gives the virial mass enclosed within the BLR, which is dominated by the black hole (e.g., Peterson et al. 1998; Kaspi et al. 2000). The validity of reverberation masses has been upheld by the detection of virial behavior in the broad line region in a subset of objects (e.g., Peterson & Wandel 1999, 2000; Onken & Peterson 2002; Kollatschny 2003), as well as the consistency of reverberation masses with other dynamical mass methods, such as stellar dynamics (Davies et al. 2006; Onken et al. 2007) and gas dynamics (Hicks & Malkan 2008). Due to the long-term nature of reverberation-mapping projects, these measurements have only been carried out for a relatively small sample of AGNs in the past: about 36 Seyferts 1s and low-luminosity quasars.

The BLR radius–luminosity correlation ($R_{\text{BLR}} \propto L^\alpha$) derived from this reverberation sample is the basis for *all* secondary techniques used to estimate black hole masses in distant AGNs (e.g., Laor 1998; Wandel, Peterson & Malkan 1999; McLure & Jarvis 2002; Vestergaard & Peterson 2006) and is an essential tool used to search for cosmological evolution of the $M_{\text{BH}} - \sigma_*$ relationship (e.g., Peng et al. 2006; Woo et al. 2008). The power of the $R_{\text{BLR}}-L$ relationship comes from the simplicity of using it to quickly estimate M_{BH} for large samples of objects, even at high redshift, using two simple measurements from a single spectrum of each object.

Peterson et al. (2004) compiled and consistently reanalyzed the database of available reverberation-mapping data for 35 AGNs, with the goal of improving the measurements of the size of the BLR and thereby improving their mass measurements. Subsequently, Kaspi et al. (2005) reanalyzed the $R_{\text{BLR}}-L$ relationship and found a power-law slope of $\alpha = 0.665 \pm 0.069$ using the optical continuum and broad $H\beta$ line. However, many of the AGNs in the sample reside in host galaxies that are comparable in luminosity to the AGN itself. Even worse, with the typically large apertures employed in reverberation-mapping campaigns (i.e. $5''0 \times 7''5$), the host-galaxy starlight contribution to the spectroscopic luminosity of any given source is substantial. Failure to account for the enhancement of the luminosity by starlight results in an artificially steep slope for the $R_{\text{BLR}}-L$ relationship, as a larger

¹ Present Address: Department of Physics and Astronomy, 4129 Frederick Reines Hall, University of California, Irvine, CA 92697; mbentz@uci.edu

² Department of Astronomy, The Ohio State University, 140 West 18th Avenue, Columbus, OH 43210; peterson, pogge@astronomy.ohio-state.edu

³ Center for Cosmology and AstroParticle Physics, The Ohio State University, 191 West Woodruff Avenue, Columbus, OH 43210

⁴ School of Physics and Astronomy and the Wise Observatory, The Raymond and Beverly Sackler Faculty of Exact Sciences, Tel-Aviv University, Tel-Aviv 69978, Israel; netzer@wise.tau.ac.il

⁵ Department of Physics and Astronomy, Robinson Hall, Tufts University, Medford, MA 02155; M.Vestergaard@tufts.edu

percentage of the luminosity in faint AGNs is contributed by the host galaxy.

A preliminary study by Bentz et al. (2006a) presented two-dimensional fits to high-resolution *HST* images of 14 reverberation-mapped AGNs, from which the host-galaxy contribution was determined. The luminosities of the 14 sources were corrected and the $R_{\text{BLR}}-L$ relationship was re-examined, resulting in a measured power-law slope of $\alpha \approx 0.5$, consistent with the naive prediction that all AGNs are simply luminosity-scaled versions of each other. In this work, we present high-resolution *HST* images of the rest of the $H\beta$ reverberation-mapped AGNs, bringing the total to 35. We improve upon our previous two-dimensional fits and reanalyze the $R_{\text{BLR}}-L$ relationship after correcting the luminosity of every AGN for the contribution from starlight. We show that these new results are consistent with those from our preliminary study, and discuss the new measurements in light of known systematic errors that may affect the slope of the $R_{\text{BLR}}-L$ relationship. Throughout this work, we will assume a standard flat Λ CDM cosmology with $\Omega_{\text{B}} = 0.04$, $\Omega_{\text{DM}} = 0.26$, $\Omega_{\Lambda} = 0.70$, and $H_0 = 70 \text{ km s}^{-1} \text{ Mpc}^{-1}$.

2. OBSERVATIONS AND DATA REDUCTION

2.1. Hubble Space Telescope

Between 2003 August 22 and 2007 January 17, we observed 30 AGNs from the reverberation-mapped sample of Peterson et al. (2004) with the *HST* Advanced Camera for Surveys (ACS). Following the failure of ACS on 2007 January 27, the remaining 5 AGNs in our sample were observed with Wide Field Planetary Camera 2 (WFPC2). The targets are listed in Table 1 and details of the observations are listed in Table 2.

For the ACS observations, each object was imaged with the High Resolution Channel (HRC) through the F550M filter ($\lambda_c = 5580 \text{ \AA}$ and $\Delta\lambda = 547 \text{ \AA}$), thereby probing the continuum while avoiding strong emission lines. The observations consisted of at least three exposures for each object, with exposure times of 120 s, 300 s, and 600 s. This method of graduating the exposure times was employed to avoid saturation of the nucleus but still obtain a reasonable signal-to-noise ratio (S/N) for the wings of the point-spread function (PSF) and the host galaxy. Each individual exposure was split into two equal sub-exposures to facilitate the rejection of cosmic rays. The WFPC2 observations were centered on the PC chip and were taken through the F547M filter, the closest analog to the ACS F550M filter. The exposure times were again graduated, however, we used steps of 5 s, 20 s, 60 s, 160 s and 300 s due to the smaller time-to-saturation afforded by the pixels in the PC chip.

The data quality frames provided by the *HST* pipeline were consulted to identify the individual saturated pixels associated with the nucleus in each exposure frame. These saturated pixels were clipped from the image and replaced by the same pixels from a non-saturated exposure after scaling them by the relative exposure times. All of the frames for each object were then summed to give one frame with an effective exposure time as listed in Table 2.

Cosmic rays were identified in the summed images with the Laplacian cosmic ray identification package L.A.Cosmic (van Dokkum 2001). Pixels in the PSF area of each image that were identified by L.A.Cosmic were excluded from the

list of affected pixels prior to cleaning with XVista.⁶ Each remaining affected pixel was replaced with the median value for the eight pixels immediately surrounding it.

Finally, the summed, cleaned ACS images were corrected for the distortions of the camera using the PyRAF routine *pydrizzle* in the STSDAS⁷ package for IRAF. The final stacked, cleaned images for all 35 AGNs are shown in Figure 1, overlaid with the spectroscopic aperture geometries from their ground-based monitoring campaigns.

2.2. MDM Observatory

Images of the reverberation-mapped sample of galaxies were also taken with the 1.3-m McGraw-Hill Telescope at MDM Observatory. Templeton, a 1024×1024 pixel CCD, was employed for the observations, giving a field-of-view (FOV) of $8'.53 \times 8'.53$ and a pixel scale of $0.50'' \text{ pixel}^{-1}$. Each galaxy was imaged through Harris *B*, *V*, and *R* filters. We focus here on the observations of the seven NGC objects that were visible from the location of MDM Observatory⁸. A log of the MDM observations for those objects is presented in Table 3. The data were reduced and combined with IRAF⁹ following standard procedures. The final *V*-band images are shown in Figure 2.

3. GALAXY DECOMPOSITIONS

The images of each of the objects were modeled with typical galaxy parameters in order to determine and accurately subtract the contribution from the central point source. The models were constructed using the two-dimensional image decomposition program Galfit (Peng et al. 2002), which fits analytic functions for the components of the galaxy, plus an additional point source for the nucleus, convolved with a user-supplied model point-spread function (PSF).

For each of the objects in this study, the final cleaned, stacked image was fit with a central PSF and a constant sky contribution, as well as host-galaxy components that were modeled using variations of the Sérsic (1968) profile,

$$\Sigma(r) = \Sigma_e \exp^{-\kappa[(r/r_e)^{1/n} - 1]} \quad (1)$$

where r_e is the effective radius of the component, Σ_e is the surface brightness at r_e , n is the power-law index, and κ is coupled to n such that half of the total flux is within r_e . Two special cases of the Sérsic function are the exponential profile ($n = 1$), often used in modeling galactic disks, and the de Vaucouleurs (1948) profile ($n = 4$), historically used for modeling galactic bulges. We modeled disk components using the exponential profile. However, we improve upon the results presented by Bentz et al. (2006a) in that we employed the more general Sérsic function for modeling bulges and we allow for additional parameters to describe other surface brightness components (such as a bar

⁶ XVISTA was originally developed as Lick Observatory Vista and is now maintained in the public domain by former Lick graduate students as a service to the community. It is currently maintained by Jon Holtzman at New Mexico State University, and is available at <http://ganymede.nmsu.edu/holtz/xvista>.

⁷ STSDAS and PyRAF are products of the Space Telescope Science Institute, which is operated by AURA for NASA.

⁸ NGC 3783 is located at a declination of -38° and was therefore not observed.

⁹ IRAF is distributed by the National Optical Astronomy Observatory, which is operated by the Association of Universities for Research in Astronomy (AURA) under cooperative agreement with the National Science Foundation.

or inner bulge component). These modifications were partially prompted by the large body of observations that find disk galaxies (of which our sample is mostly comprised) are more accurately described with bulge profiles that have $n < 4$ (e.g. Kormendy & Bruzual 1978; Shaw & Gilmore 1989; Andredakis & Sanders 1994; Peng et al. 2002).

There is a paucity of archival stellar images with the HRC through the F550M filter, and so simulated PSFs were created using the TinyTim package (Krist 1993) which models the optics of *HST* plus the specifics of the camera and filter system. We tested our fits using a white dwarf image from the *HST* archive as the PSF model (GO 10752, PI Lallo). Unfortunately, the image did not have the extremely high dynamic range necessary for a good fit when compared to these bright AGNs.

Many of the nearest galaxies in this sample fill the FOV of the ACS HRC, and so the sky contribution could not simply be measured from the edges of the images. Rather, the sky level was iteratively determined, starting with an estimate of the sky brightness from the ACS Instrument Handbook as the initial input. The sky value was held fixed while additional parameters were fit to the galaxy. If the estimated sky value was too low, the Sérsic index for the bulge would run up to the maximum allowed value, punching a “hole” in the nucleus of the image. If the estimated sky value was too high, the Sérsic index could run down to zero, causing Galfit to crash. A sky value intermediate to these two situations was chosen such that the residuals and χ^2 values were minimized. Once a preliminary fit was achieved, the sky value was checked and adjusted if necessary, after which the galaxy parameters were re-fit. This is an improvement over our previous work, where the sky contribution was assumed to be negligible compared to the bright host galaxies of the 14 AGNs in that sample, especially as our expanded sample includes several AGNs that are significantly brighter than their host galaxies.

All of the images required at least one galaxy component in addition to the sky and central PSF. Most required two, and a few required three or more to fit an additional component, such as a bar. Several of the bright AGNs required a small (< 2 pixel effective radius) component to help account for PSF mismatch between the AGN and the model PSF (for a full discussion of PSF variations and mismatches in *HST* imaging, see Krist 2003; Kim et al 2008). Extraneous objects in the field were also fit, such as intervening stars or galaxies, to ensure that the proper distribution of light was attributed to the AGN host galaxy. Compared to the simple galaxy decompositions for the 14 objects in our previous work, the surface brightness residuals and nominal χ^2 fitting values have been significantly reduced, showing that the fits presented here more accurately model the underlying host galaxy surface brightness distributions. For example, the average magnitude of the residuals for 3C 120 was reduced by a factor of ~ 4 and the χ^2 value was reduced by a factor of ~ 5 .¹⁰ In all cases, the fits have been encouraged to attribute more flux to the sky background and PSF components, resulting in conservative flux values for the host-galaxy components. The quoted brightness for each of the host galaxy components may

be somewhat underestimated as a result.

For the seven NGC objects with MDM images, the *V*-band MDM images were each fit with an exponential disk and a Sérsic bulge. The effective radius of the disk component was then translated to the pixel scale of the HRC camera and held fixed during the fits to the *HST* image. As the seeing in the MDM images was typically on the order of $\sim 2''$, the PSF and the bulge of the galaxy were blurred together. Thus, the bulge fits from the ground-based images were held to be unreliable and were instead determined from the *HST* images.

Table 4 presents the details of the fits to the *HST* images. The input image, Galfit model, residuals, and one-dimensional surface brightness cut for each of the 35 host galaxies are presented in Figure 3. Global parameters including the total galaxy luminosity and the ratio of the bulge luminosity to the total luminosity (B/T) were determined from the fits and are listed in Table 5. Also listed in Table 5 are the morphological classifications of the galaxies, several of which were listed in the NASA/IPAC Extragalactic Database (NED). For those objects without morphological classifications (objects marked with a flag in Table 5), the parameters fit to the galaxy images were used to determine the appropriate classification based on the de Vaucouleurs (1959) classification scheme. The index k for the subtype of the elliptical galaxies in the sample was calculated as $k = 10(1 - b/a)$ and rounded to the nearest whole number. Spiral galaxies were classified based on their B/T compared to the mean of the distributions of B/T as a function of morphological type in Figure 6 of Kent (1985).

As discussed by Peng et al. (2002), degeneracy between galaxy components and between parameters within components is typically an issue when fitting analytic models to galaxy images. This is certainly the case with the sample of objects presented here. The bright AGNs in the galaxy centers are degenerate with the concentration of the bulge (the Sérsic index n), especially when the bulge component is rather compact. As discussed above, many of these images have the added complication of having a somewhat uncertain sky contribution which also affects n as well as the scale length of the disk. Interpreting the specific details of the galaxy fits presented here is therefore difficult. The relatively low n values for the galaxy bulges in this sample certainly seem to agree with the works referenced above that find $n < 4$ for most spiral galaxies. However, the actual n values may be somewhat underestimated as a result of our conservative fits that attribute more flux to the AGN and the sky background. A quick glance through the galaxy fits in Table 4 might lead one to speculate on the prevalence of pseudobulges versus classical bulges in this sample. Per the discussion by Kormendy & Kennicutt (2004), however, the lack of dynamical info for the host galaxies in this sample as well as the uncertainty in interpreting the galaxy fitting parameters complicates any conclusions that might be drawn about the origins of the bulges in these galaxies.

Several of the fits listed in Table 4 include components noted as being an “inner bulge” or “bar”. The classifications for these extra components are simply morphological, with a “bar” typically having a more elongated shape than an “inner bulge”. Bars themselves tend to have an inner bulbous component, so the “inner bulges” listed here may actually be related to bars themselves (Peng et al. 2002). We do not have kinematic information to determine which of these additional components may be physically distinct from the bulge or disk of the host galaxy. The fact that additional components are

¹⁰ The actual value of χ^2 is not particularly meaningful when related to galaxy fitting. The relative χ^2 values for different fits to the same image are more relevant, with smaller values denoting “better” fits. Details of the calculation and interpretation of χ^2 values can be found in the FAQ section of Chien Peng’s Galfit home page, <http://users.ociw.edu/peng/work/galfit/galfit.html>

required to achieve a better fit is likely in many cases to simply be the result of attempting to fit analytic functions to resolved galaxies with strong substructure. In particular, areas with dust obscuration and spiral arm structure are difficult to properly fit with analytic functions. As our main goal is to determine the PSF contribution as accurately as possible and to create “nucleus-free” images of these galaxies, we do not discuss here the origin or meaning of these additional components in the galaxy fits.

4. FLUX MEASUREMENTS

Once the fit to each galaxy was finalized, the sky and PSF components were subtracted, leaving a nucleus-free image of each host galaxy. Each image was overlaid with the typical aperture used in the ground-based monitoring program(s), at the typical orientation and centered on the position of the AGN (see Table 6). The counts within the aperture were summed and converted to f_λ flux density units ($\text{ergs s}^{-1} \text{cm}^{-2} \text{\AA}^{-1}$) using the *HST* keyword PHOTFLAM and the effective exposure time for each object.

Color corrections to the observed galaxy flux densities were calculated using a model bulge spectrum (Kinney et al. 1996) to account for the difference between the effective wavelength of the *HST* filter and restframe 5100 \AA for each object. The model bulge spectrum was redshifted to the distance of each AGN host galaxy and reddened by the appropriate Galactic extinction. The redshifted, reddened models were convolved with the *HST* filter response using the *synphot* package in the IRAF/STSDAS library and subsequently scaled to the appropriate flux level as measured from the *HST* images. Finally, the observed flux at rest-frame 5100 \AA was measured from the model. The flux density measured directly from the nucleus-free *HST* images and the color-corrected flux and luminosity at 5100 \AA , are listed in Table 7. We note that the color correction method outlined above is different from that employed previously, and again results in more conservative host galaxy flux values.

The final step requires subtraction of the galaxy flux from the mean flux measured during a monitoring campaign, and leaves only the flux contribution from the AGN itself. The corresponding AGN luminosities were calculated and corrected for Galactic absorption using the Schlegel et al. (1998) A_B values listed in NED and the extinction curve of Cardelli et al. (1989), adjusted to $A_V/E(B-V) = 3.1$. The starlight-corrected AGN fluxes and luminosities are listed in Table 8 with their corresponding $H\beta$ lags. The numbers in bold font are the weighted averages of multiple measurements for a particular object.

Ongoing work with this sample of objects has resulted in some updates to the reverberation database presented by Peterson et al. (2004) and fit by Kaspi et al. (2005). In addition, a few data sets require cautionary or explanatory notes. Specifically, we note the following:

- NGC 3516: The light curves presented by Wanders et al. (1993) were not measured from data with an absolute flux calibration. Therefore, while we have included this object, it should be regarded with caution as the spectroscopic luminosity is not well-determined.
- NGC 4151: The aperture used in the monitoring campaign described by Maoz et al. (1991) is $20'' \times 28''$,

which is larger than the field of view of the HRC camera. In addition, the Kaspi et al. (1996) data set has a rather unconstrained time lag that is consistent with zero once the monotonic increase in the continuum and line flux is removed (see Metzroth et al. 2006 for a full discussion). Both of these data sets for NGC 4151 have been superseded by the results reported by Bentz et al. (2006b), which we include here in their stead.

- PG 1211+143: Peterson et al. (2004) note that all of the lag measurements for this object are rather unconstrained. For consistency with past analyses of the $R_{\text{BLR}}-L$ relationship, we have included the $H\beta$ lag for PG1211 here, but it should be regarded with caution.
- NGC 4593: The campaign originally described by Dietrich et al. (1994) and reanalyzed by Onken et al. (2003) gives an $H\beta$ lag that is consistent with zero. The results for NGC 4593 have been superseded by those reported by Denney et al. (2006), which we include here.
- IC 4329A: According to Peterson et al. (2004), the light curves for this object are very noisy and of poor quality, resulting in an $H\beta$ lag measurement that is highly suspect as well as being consistent with zero. In addition, IC 4329A is an edge-on galaxy with a prominent dust disk along the line of sight to the AGN, resulting in a substantial amount of internal reddening. The presence of the strong dust lane across the galaxy in the *HST* images also presented problems for the host galaxy fitting. Because this object has both an unreliable lag measurement and an unreliable luminosity measurement, we have excluded it from the analysis of the $R_{\text{BLR}}-L$ relationship.
- Mrk 279: The monitoring campaign described by Maoz et al. (1990) used an aperture of $20'' \times 28''$, which exceeds the HRC field of view. We include here only the results for Mrk 279 reported by Santos-Lleó et al. (2001).
- NGC 5548: The aperture of $20'' \times 28''$ used in the campaign described by Netzer et al. (1990) is larger than the field of view of the HRC camera. We include here the 14 individual measurements reported by Peterson et al. (2002) and Bentz et al. (2007).
- PG 2130+099: For some time now, the $H\beta$ lag measured for this object has been suspected of being artificially long. This suspicion has been confirmed by Grier et al. (2008), who have recently reanalyzed the data set originally presented by Kaspi et al. (1996) and find that the lag measured from these data is erroneous due to undersampling of the light curves and long-term secular changes in the equivalent width of the broad $H\beta$ emission line. In addition, Grier et al. present a new monitoring campaign for this object that was undertaken at MDM Observatory in the fall of 2006, and report a new $H\beta$ lag measurement. We include only the Grier et al. result in our analysis here.

5. CONSISTENCY CHECKS

The difficulty of fitting surface brightness profiles with multiple analytic functions is widely appreciated. While the GALFIT program we have used works remarkably well and

represents the state of the art, there are still some ambiguities that cannot always be easily resolved: at a sufficiently large distance, for example, it is simply impossible, even with the high angular resolution of the ACS HRC, to separate a point source AGN and a luminous bulge with a high Sérsic index. In addition, several parameters that are used in the surface brightness fits can be very degenerate, leading to difficulties in disentangling the results from many different parameter combinations when no other information is available. All this may result in systematic uncertainties that are larger than the formal errors (of order 10%) that are listed in Table 7. There are, however, a number of consistency checks that provide robust upper limits on the host galaxy contributions and can help to remove some of this degeneracy. Indeed, our decision to revisit the Bentz et al. (2006a) fits was motivated at least in part by such considerations.

The simplest consistency check is that the AGN flux must always remain non-negative: the host galaxy flux at any wavelength must be less than the observed brightness of the combined AGN and host galaxy when the AGN is in its faintest observed state. We have compared the measured host galaxy fluxes to the individual monitoring light curves for each of the objects in this sample to ensure that this consistency check is always satisfied. A second consistency check is provided by spectral decomposition, i.e., by fitting multiple components of a spectrum rather than an image. Our experience, however, is that spectral decomposition is certainly no less ambiguous than image decomposition, but when carefully done with very good data, shows reasonable consistency (e.g., the modeling of the optical spectrum of NGC 5548 by Denney et al. 2008 yields a host galaxy flux in agreement with the value we find here). A third check, which applies at least in the case of the higher luminosity AGNs, is that the total luminosity of the host galaxy, based on the model fit, must not exceed the luminosity of known bright normal galaxies. Our galaxy fits seem to be consistent with this constraint as well. The brightest host galaxy in the sample is PG 1226+023, also known as 3C 273, which has $M_V \approx -23.8$, and the second brightest with $M_V \approx -23.2$ is PG 1700+518, the most distant AGN in the sample at $z = 0.292$. Compared to the Trentham et al. (2005) field galaxy luminosity function, the derived host galaxy brightnesses for the AGNs in this study seem to be fairly typical.

A more subtle consistency check on the host-galaxy contribution to the ground-based monitoring luminosity comes from photoionization considerations, namely that the ratio of emission-line to AGN continuum flux (i.e., the emission-line equivalent width) ought not to vary wildly in time. For an optically thick medium, the equivalent width of an emission line is expected to stay relatively constant. Some variations are possible, either due to changes in the continuum shape or if there is an optically thin BLR component. Significant variations in the equivalent width can follow a large-amplitude change in the incident continuum flux, however, the variations should stabilize and return to a relatively constant value shortly thereafter. In addition, secular trends in the equivalent width can occur over dynamical timescales, which are much longer than reverberation timescales. If too much flux is attributed to the host galaxy of an object, the AGN continuum will be underestimated and the fractional variations of the $H\beta$ emission-line equivalent width will become consistently large, in contrast to the variations that can be expected from the discussion above. An important point to note is that the relevant equivalent width measure is the ratio of emission-line flux at some time, t , relative to the continuum flux at

some earlier time, $t - \tau$, where τ is the emission-line time delay from reverberation measurements (e.g., Pogge & Peterson 1992; Gilbert & Peterson 2003).

To illustrate this check, we consider the specific case of 3C 120, which we selected because the starlight contribution changed the most from our previous work, decreasing by a factor of almost 3. In Figure 4 we show the equivalent width of the $H\beta$ emission line (in the observed frame) as a function of time, based on the light curve from Peterson et al. (1998). Each measurement of the emission-line flux, $F_{H\beta}(t)$, was divided by an interpolated value of the continuum flux density, $F_\lambda(t - \tau)$, with an observed-frame emission-line lag of $\tau = 39.4$ days. We note in passing that the first few emission-line measurements are disregarded since there is no corresponding continuum information. The open circles in Figure 4 refer to the original data, without any correction for starlight. The triangles are the new equivalent width measurements for the same emission line fluxes, but in this case the continuum measurements have been adjusted by the host-galaxy value from Bentz et al. (2006a). The large equivalent widths and consistently rapid variations strongly suggest that this value of the host-galaxy correction is too large, as the fractional variations of the remaining AGN continuum must be enormous. The filled circles show the equivalent widths based on the revised value of the host-galaxy contribution given here in column (3) of Table 7. In this case, the values of the equivalent widths are much more reasonable (i.e., typical of quasars, where host-galaxy contamination is negligible) and the variations are much more moderate, indicating that the host-galaxy measurement provided here is more accurate than the measurement based on the more simplistic host-galaxy models utilized by Bentz et al.

For all 35 objects in the sample, the galaxy fits in §3 were carried out independently from the consistency checks discussed above. The more conservative approach we have applied to the galaxy fits here results in good agreement with the expectations from all of these consistency checks for the 35 objects in the sample. Of the 14 objects included in our preliminary study, three objects have starlight contributions through their monitoring apertures that changed by more than 35% as measured directly in counts from the nucleus-free images, one of them being 3C 120, as discussed above. In all cases, the decreased residuals and χ^2 values from the new fits, combined with the results of the consistency checks, lead us to believe that the galaxy fits in this work more accurately describe the underlying host-galaxy surface brightness distributions than the simplistic fits determined by Bentz et al. (2006a).

6. THE RADIUS–LUMINOSITY RELATIONSHIP

We have calculated several fits to the $R_{\text{BLR}}-L$ relationship for the full sample of starlight-corrected AGNs. For this analysis, the time lags have been restricted to the $H\beta$ lag only. This is different from the method employed by Kaspi et al. (2005), where the $R_{\text{BLR}}-L$ fits were also calculated for the Balmer-line average, which sometimes included $H\alpha$ and/or $H\gamma$. There is one exception to this, however, in that PG 0804+761 does not have a reliable $H\beta$ measurement, but it does have reliable measurements for $H\alpha$ and $H\gamma$. We use the lag measurement for $H\alpha$ here, as it is the more reliable of the two measurements available.

In the same way as Kaspi et al., we have made the distinction of treating each separate $H\beta$ lag measurement of an object individually, as well as taking the mean of multiple mea-

measurements weighted by the average of the positive and negative errors. We tested the differences between weighting measurements by the average of their errors, by taking only the positive errors, and by taking the errors toward the fit in the manner of Kaspi et al. (2005). We find the differences in these weighting methods to be at the 2% level, and therefore negligible.

While the two above methods for sampling the reverberation-mapping database are relatively straightforward to carry out, various issues arise when determining the $R_{\text{BLR}}-L$ relationship from these datasets. In the first case, where every measurement is given equal weight, those objects that have many measurements (such as NGC 5548) will have more weight in the determination of the slope than objects with single measurements. In the second case, where multiple measurements are averaged together, each object has the same weight but information is being lost in the average because we do not, in fact, expect the luminosity and lag to be the same in multiple campaigns during different years. It is unclear as to the correct way to combine multiple measurements in this case.

A somewhat more laborious method of sampling the reverberation-mapping database is to randomly select one pair of radius and luminosity measurements for every object, from which selection the relationship is fit, and to build up a large number ($N = 1000$) of individual realizations through Monte Carlo techniques. This method gives equal weight to every object and circumvents the problem of how to combine multiple measurements for any particular object. In addition to the two simpler methods outlined above, we employ this method in the determination of the $R_{\text{BLR}}-L$ relationship, but we consider this method to be superior to the others.

Three different fitting routines were used to calculate the relationship between the size of the BLR and the optical luminosity:

1. FITEXY (Press et al. 1992), which estimates the parameters of a straight-line fit through the data including errors in both coordinates. FITEXY numerically solves for the minimum orthogonal χ^2 using an iterative root-finding algorithm. We include intrinsic scatter similar to Kaspi et al. (2005) after the prescription of Tremaine et al. (2002). Namely, the fractional scatter listed in Table 9 is the fraction of the measurement value of R_{BLR} (not the error value) that is added in quadrature to the error value so as to obtain a reduced χ^2 of 1.0.
2. BCES (Akritas & Bershady 1996), which attempts to account for the effects of errors on both coordinates in the fit using bivariate correlated errors, including a component of intrinsic scatter. We adopt the bootstrap of the bisector value following Kaspi et al. (2005), with $N = 1000$ iterations.¹¹
3. GaussFit (McArthur et al. 1994), which implements generalized least-squares using robust Householder Orthogonal Transformations (Jefferys 1980, 1981) to solve the

¹¹ We note that the errors on L listed in the table are formal measurement errors that, in most cases, are far smaller than the actual observed variations even in one campaign. Therefore, we also tested BCES correlations that assume an uncertainty of 0.1-0.15 dex on L . The results are similar to the ones obtained by our realization method and hence not listed separately.

non-linear equations of condition for the problem of errors in both coordinates. No attempt is made to account for intrinsic scatter.

Table 9 lists the fit parameters determined for a $R_{\text{BLR}}-L$ relationship of the following form:

$$\log(R_{\text{BLR}}) = K + \alpha \log(\lambda L_{\lambda}(5100\text{\AA})) \quad (2)$$

where α is the slope of the power-law relationship between R_{BLR} and $\lambda L(5100\text{\AA})$, and K is the zero point. The calculated power-law slopes to the $R_{\text{BLR}}-L$ relationship range from 0.499 ± 0.042 to 0.554 ± 0.050 , depending on the particular algorithm used for fitting the relationship and how the objects with multiple measurements are treated.

We prefer the Monte Carlo random sampling method outlined above as the proper way to treat objects with multiple individual measurements. And for its manner of dealing with intrinsic scatter within the data set, we prefer the BCES bootstrap method. The combination of these methods gives $K = -21.3^{+2.9}_{-2.8}$ and $\alpha = 0.519^{+0.063}_{-0.066}$, our best estimate for the form of the $R_{\text{BLR}}-L$ relationship at this time.

Figure 5 shows the $R_{\text{BLR}}-L$ relationship after correcting the full sample of reverberation-mapped AGNs for the contribution from host-galaxy starlight. The top panel of Figure 5 shows each individual data point from the monitoring campaigns included here, and the bottom panel shows a single data point for each individual AGN determined by the weighted average of multiple measurements. The solid lines show the best fit to the $R_{\text{BLR}}-L$ relationship described above.

7. DISCUSSION

Throughout this work, we have improved upon our original methods by using more accurate and more conservative profiles to model the host galaxy components, as well as a more conservative color correction method, all resulting in conservative measurements of the host galaxy starlight as measured for every object contributing to the $R_{\text{BLR}}-L$ relationship. Even so, the best fit to the relationship has not changed significantly from that presented by Bentz et al.: $0.519^{+0.063}_{-0.066}$ compared to the previous value of 0.518 ± 0.039 . It would appear that given reasonably high-resolution, unsaturated images of AGN host galaxies and reasonable fits to the host galaxy surface brightness profiles, the AGN luminosity can be corrected for the contamination from starlight fairly accurately.

AGN BLRs can be modeled assuming the central radiation field is the only source of heating and ionization of the gas. The simplest, most naive assumption is that all BLRs are made of identical clouds, with the same density, column density, composition and ionization parameter. In addition, the radiation from all AGNs can be assumed to have the same spectral energy distribution (SED). This results in the prediction that $R_{\text{BLR}} \propto L^{0.5}$. Any changes in the BLR gas distribution or the AGN SED, especially those associated with source luminosity, will result in a different slope. In fact, AGNs have been observed to have different SEDs as a function of luminosity (e.g., Mushotzky & Wandel 1989; Zheng & Malkan 1993). It is therefore interesting that our present work based on the results from several reverberation-mapping campaigns produces a slope for the $R_{\text{BLR}}-L$ relationship that is consistent with the naively expected slope of 0.5, and that, to a first approximation, brighter AGNs are simply ‘‘scaled up’’ versions of fainter AGNs.

Removing the host-galaxy starlight component reduces the

scatter¹² in the $R_{\text{BLR}}-L$ relationship, from 39–44% as found by the best-fit FITEXY results from Kaspi et al. (2005) to 34–40% as found here. It also flattens the slope of the relationship considerably. This has the overall effect of biasing samples that used previous versions of the $R_{\text{BLR}}-L$ relationship to estimate black hole masses. The host-galaxy starlight is often removed through spectroscopic decomposition of single-epoch spectra before the size of the BLR radius is estimated from the continuum luminosity. However, it is crucial to use a $R_{\text{BLR}}-L$ relationship in which the objects providing the calibration are *also* corrected for host-galaxy starlight, which we have provided here. Compared with the best-fit relationship of Kaspi et al. (2005), we find that the calibration of the $R_{\text{BLR}}-L$ relationship presented here results in black hole masses that are $\sim 30\%$ smaller at $L = 10^{46}$, $\sim 50\%$ larger at $L = 10^{44}$, and a factor of ~ 3 larger at $L = 10^{42}$.

At the low-luminosity end ($L \lesssim 10^{43}$), there may still be some uncertainty as to the behavior of the $R_{\text{BLR}}-L$ relationship. In the current sample of objects with reverberation-mapping results, there are somewhat fewer objects at lower-luminosity and they have larger uncertainties than the other, higher-luminosity objects in the sample. It should be kept in mind that the lower-luminosity objects were, in general, the first targets of ground-based monitoring campaigns due to their relatively low redshifts and high apparent brightnesses. The larger uncertainties in their measurements is partially due to the less-rigorous control over observational factors in those early monitoring campaigns (such as observing cadence, spectral resolution, detector efficiency, etc.) simply because there was a lack of experience in this field at that time. The problems of small sample size and relatively larger uncertainties for lower luminosity objects will soon be mitigated by two independent reverberation mapping campaigns which have been recently carried out at MDM Observatory and at Lick Observatory and targeted the low-luminosity end of the relationship. Preliminary results from the MDM campaign promise to replace several measurements, as was done in the case of NGC 4593 (Denney et al. 2006) and NGC 4151 (Bentz et al. 2006b) in the 2005 MDM campaign. And preliminary results from the Lick campaign promise to add several new objects to the low-luminosity end of the $R_{\text{BLR}}-L$ relationship (e.g., Bentz et al. 2008).

Internal reddening is known to be a problem in some of the very nearest, and lower-luminosity, objects in the current reverberation sample. For example, NGC 3227 is known to have substantial internal reddening compared to most of the other objects in the current sample and should therefore require one of the largest reddening corrections. Crenshaw et al. (2001) determined a reddening curve for NGC 3227 and find that at 5100 \AA , $A_{\lambda}/E(B-V) = 3.6$ and $E(B-V) = 0.18$. This implies an extinction at 5100 \AA of 0.65 mag, which, if corrected for, would increase the luminosity here by a factor of 1.8, or 0.26 dex, moving the location of NGC 3227 in the bottom panel of Figure 5 from slightly left of the best fit $R_{\text{BLR}}-L$ relationship to right on top of it. As we do not have similar corrections for the other objects in this sample, we do not apply the reddening correction for NGC 3227 in our determination of the $R_{\text{BLR}}-L$ relationship. However, based on the magnitude of the correction determined for NGC 3227, there does not seem to be any reason to expect that correcting all

the sources for internal reddening will have much effect on the slope of the $R_{\text{BLR}}-L$ relationship.

An obvious issue that may also be addressed with the galaxy fits that we have presented in this work is the relationship between black hole mass and host galaxy bulge luminosity (or mass; Kormendy & Richstone 1995; Magorrian et al. 1998). We discuss this relationship for the AGNs in our sample in a related manuscript (Bentz et al. 2009).

8. SUMMARY

We have presented high-resolution *HST* images of the 35 AGNs with optical reverberation-mapping results. The host galaxy of each object was fit with typical galaxy components, and a nucleus-free image of each AGN host galaxy was created. From these nucleus-free images, we measured the starlight contribution to the ground-based spectroscopic luminosity measured at rest-frame 5100 \AA . We then removed the starlight contamination from the AGN luminosities and re-examined the $R_{\text{BLR}}-L$ relationship. We find a best fit slope of $\alpha = 0.519^{+0.063}_{-0.066}$, consistent with the results from our preliminary study, and still suggesting that all AGNs are simply luminosity-scaled versions of each other. We discuss several consistency checks that support our galaxy modeling results. Various systematics, such as the smaller number and larger uncertainties of measurements at lower luminosities as well as internal reddening, are discussed in the context of their effect on the $R_{\text{BLR}}-L$ relationship.

We thank the anonymous referee for helpful comments and suggestions which improved the presentation of this manuscript. We also thank Chien Peng for his excellent program Galfit, which enabled us to carry out this study, and for helpful conversations regarding the galaxy fitting. This work is based on observations with the NASA/ESA *Hubble Space Telescope*. We are grateful for support of this work through grants *HST* GO-9851, GO-10516, and GO-10833 from the Space Telescope Science Institute, which is operated by the Association of Universities for Research in Astronomy, Inc., under NASA contract NAS5-26555, and by the NSF through grant AST-0604066 to The Ohio State University. M.B. gratefully acknowledges support from the NSF through grant AST-0548198 to the University of California, Irvine. This research has made use of the NASA/IPAC Extragalactic Database (NED) which is operated by the Jet Propulsion Laboratory, California Institute of Technology, under contract with the National Aeronautics and Space Administration and the SIMBAD database, operated at CDS, Strasbourg, France.

¹² Throughout this manuscript, “scatter” refers to the $1-\sigma$ deviation from the best fit $R_{\text{BLR}}-L$ relationship.

REFERENCES

- Akritas, M. G., & Bershady, M. A. 1996, *ApJ*, 470, 706
 Andredakis, Y. C., & Sanders, R. H. 1994, *MNRAS*, 267, 283
 Bentz, M. C., Peterson, B. M., Pogge, R. W., Vestergaard, M., & Onken, C. A. 2006a, *ApJ*, 644, 133
 Bentz, M. C., et al. 2006b, *ApJ*, 651, 775
 —. 2007, *ApJ*, 662, 205
 —. 2008, *ApJ*, 689, L21
 Bentz, M. C., Peterson, B. M., Pogge, R. W., & Vestergaard, M. 2009, *ApJ*, submitted
 Blakeslee, J. P., Lucey, J. R., Barris, B. J., Hudson, M. J., & Tonry, J. L. 2001, *MNRAS*, 327, 1004
 Blandford, R. D., & McKee, C. F. 1982, *ApJ*, 255, 419
 Cardelli, J. A., Clayton, G. C., & Mathis, J. S. 1989, *ApJ*, 345, 245
 Collier, S. J., et al. 1998, *ApJ*, 500, 162
 Crenshaw, D. M., Kraemer, S. B., Bruhweiler, F. C., & Ruiz, J. R. 2001, *ApJ*, 555, 633
 Davies, R. I., et al. 2006, *ApJ*, 646, 754
 de Vaucouleurs, G. 1948, *Annales d'Astrophysique*, 11, 247
 —. 1959, *Handbuch der Physik*, 53, 275
 Denney, K., et al. 2006, *ApJ*, 653, 152
 —. 2008, *ApJ*, in press (astro-ph/0810.3234)
 Dietrich, M., et al. 1994, *A&A*, 284, 33
 —. 1998, *ApJS*, 115, 185
 Ferrarese, L., & Merritt, D. 2000, *ApJ*, 539, L9
 Gebhardt, K., et al. 2000, *ApJ*, 539, L13
 Gilbert, K. M., & Peterson, B. M. 2003, *ApJ*, 587, 123
 Grier, C., et al. 2008, *ApJ*, 688, 837
 Hicks, E. K. S., & Malkan, M. A. 2008, *ApJS*, 174, 31
 Jefferys, W. H. 1980, *AJ*, 85, 177
 —. 1981, *AJ*, 86, 149
 Kaspi, S., Maoz, D., Netzer, H., Peterson, B. M., Vestergaard, M., & Jannuzi, B. T. 2005, *ApJ*, 629, 61
 Kaspi, S., Smith, P. S., Netzer, H., Maoz, D., Jannuzi, B. T., & Giveon, U. 2000, *ApJ*, 533, 631
 Kaspi, S., et al. 1996, *ApJ*, 470, 336
 Kent, S. M. 1985, *ApJS*, 59, 115
 Kim, M., Ho, L. C., Peng, C. Y., Barth, A. J., & Im, M. 2008, *ApJS*, 179, 283
 Kinney, A. L., Calzetti, D., Bohlin, R. C., McQuade, K., Storchi-Bergmann, T., & Schmitt, H. R. 1996, *ApJ*, 467, 38
 Kollatschny, W. 2003, *A&A*, 407, 461
 Kormendy, J., & Bruzual, A. G. 1978, *ApJ*, 223, L63
 Kormendy, J., & Richstone, D. 1995, *ARA&A*, 33, 581
 Kormendy, J., & Kennicutt, R. C. 2004, *ARA&A*, 42, 603
 Krist, J. 1993, in *ASP Conf. Ser. 52: Astronomical Data Analysis Software and Systems II*, 536
 Krist, J. 2003, *ACS Instrument Science Report*, ISR 2003-06
 Laor, A. 1998, *ApJ*, 505, L83
 Magorrian, J., et al. 1998, *AJ*, 115, 2285
 Maoz, D., et al. 1990, *ApJ*, 351, 75
 —. 1991, *ApJ*, 367, 493
 McArthur, B., Jefferys, W., & McCartney, J. 1994, *Bulletin of the American Astronomical Society*, 26, 900
 McLure, R. J., & Jarvis, M. J. 2002, *MNRAS*, 337, 109
 Metzroth, K. G., Onken, C. A., & Peterson, B. M. 2006, *ApJ*, 647, 901
 Mushotzky, R. F., & Wandel, A. 1989, *ApJ*, 339, 674
 Netzer, H., et al. 1990, *ApJ*, 353, 108
 Onken, C. A., & Peterson, B. M. 2002, *ApJ*, 572, 746
 Onken, C. A., Peterson, B. M., Dietrich, M., Robinson, A., & Salamanca, I. M. 2003, *ApJ*, 585, 121
 Onken, C. A., et al. 2007, *ApJ*, 670, 105
 Peng, C. Y., Ho, L. C., Impey, C. D., & Rix, H. 2002, *AJ*, 124, 266
 Peng, C. Y., Impey, C. D., Rix, H.-W., Kochanek, C. S., Keeton, C. R., Falco, E. E., Lehar, J., & McLeod, B. A. 2006, *ApJ*, 649, 616
 Peterson, B. M. 1993, *PASP*, 105, 247
 Peterson, B. M., & Wandel, A. 1999, *ApJ*, 521, L95
 —. 2000, *ApJ*, 540, L13
 Peterson, B. M., Wanders, I., Bertram, R., Hunley, J. F., Pogge, R. W., & Wagner, R. M. 1998, *ApJ*, 501, 82
 Peterson, B. M., et al. 2000, *ApJ*, 542, 161
 —. 2002, *ApJ*, 581, 197
 —. 2004, *ApJ*, 613, 682
 Pogge, R. W., & Peterson, B. M. 1992, *AJ*, 103, 1084
 Press, W. H., Teukolsky, S. A., Vetterling, W. T., & Flannery, B. P. 1992, *Numerical recipes in FORTRAN. The art of scientific computing* (Cambridge: University Press, 2nd ed.), 660
 Russell, D. G. 2003, astro-ph/0310284
 Salamanca, I., et al. 1994, *A&A*, 282, 742
 Santos-Lleó, M., et al. 1997, *ApJS*, 112, 271
 —. 2001, *A&A*, 369, 57
 Schlegel, D. J., Finkbeiner, D. P., & Davis, M. 1998, *ApJ*, 500, 525
 Sersic, J. L. 1968, *Atlas de galaxias australes* (Cordoba, Argentina: Observatorio Astronomico, 1968)
 Shaw, M. A., & Gilmore, G. 1989, *MNRAS*, 237, 903
 Shields, J. C., Ferland, G. J., & Peterson, B. M. 1995, *ApJ*, 441, 507
 Stirpe, G. M., et al. 1994, *ApJ*, 425, 609
 Tremaine, S., et al. 2002, *ApJ*, 574, 740
 Trentham, N., Sampson, L., & Banerji, M. 2005, *MNRAS*, 357, 783
 van Dokkum, P. G. 2001, *PASP*, 113, 1420
 Vestergaard, M., & Peterson, B. M. 2006, *ApJ*, 641, 689
 Wandel, A., Peterson, B. M., & Malkan, M. A. 1999, *ApJ*, 526, 579
 Wanders, I., et al. 1993, *A&A*, 269, 39
 Winge, C., Peterson, B. M., Horne, K., Pogge, R. W., Pastoriza, M. G., & Storchi-Bergmann, T. 1995, *ApJ*, 445, 680
 Winge, C., Peterson, B. M., Pastoriza, M. G., & Storchi-Bergmann, T. 1996, *ApJ*, 469, 648
 Woo, J.-H., Treu, T., Malkan, M. A., & Blandford, R. D. 2008, *ApJ*, 681, 925
 Zheng, W., & Malkan, M. A. 1993, *ApJ*, 415, 517

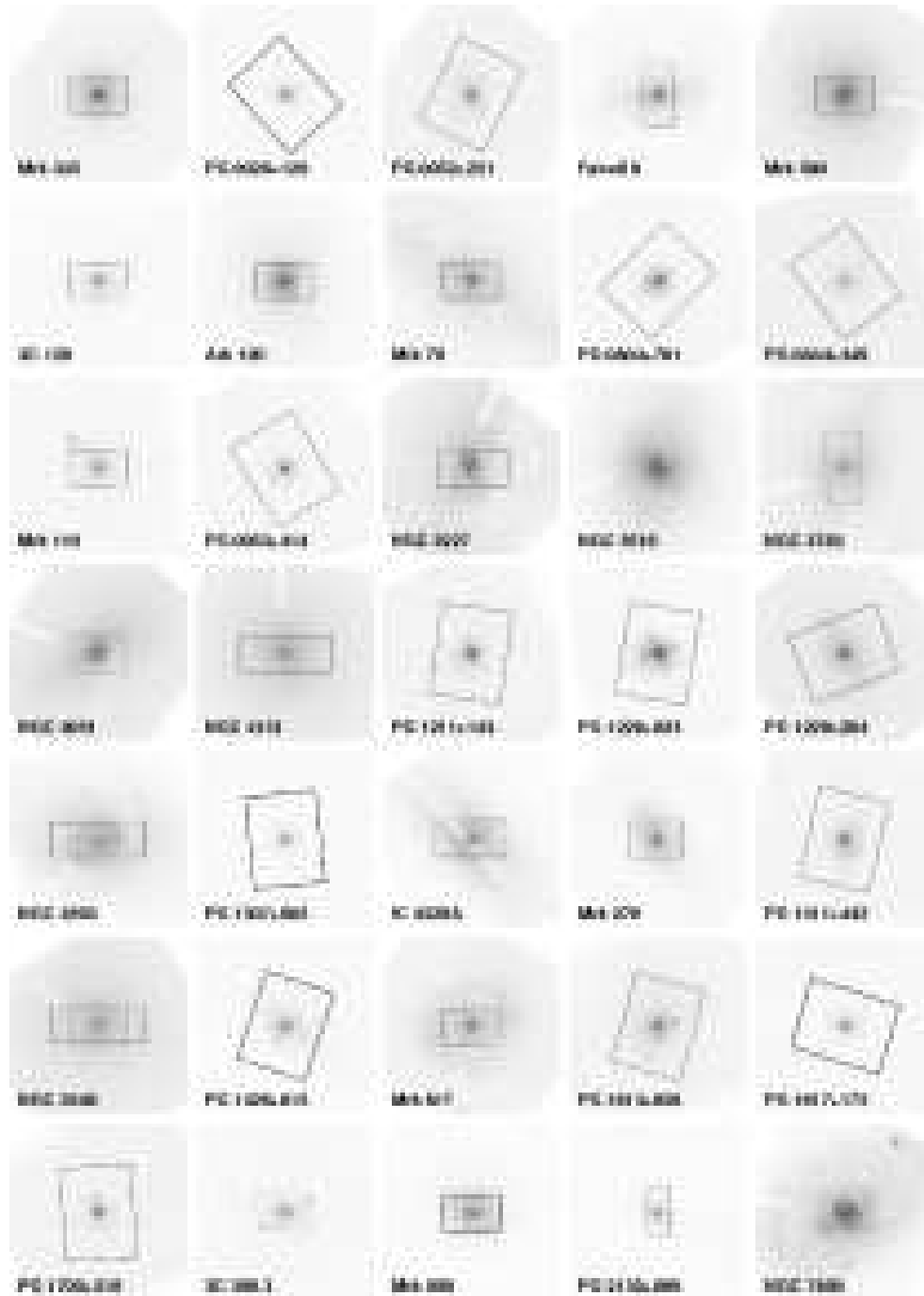


FIG. 1.— The final stacked images for the full sample of 35 reverberation-mapped AGNs with *HST* imaging. The ground-based spectroscopic monitoring apertures are overlaid. Each image is $25'' \times 25''$, with north up and east to the left.

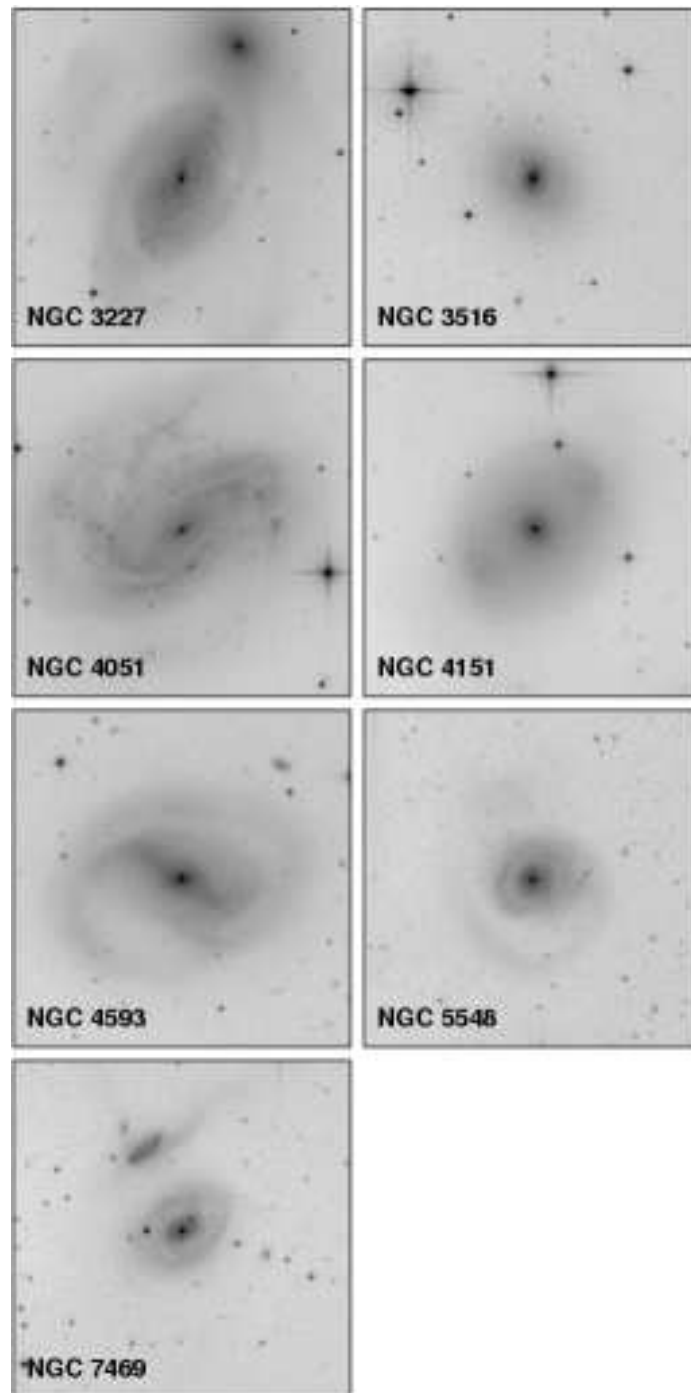


FIG. 2.— V-band images of the seven NGC objects in the reverberation-mapped sample that are visible from MDM Observatory. Each image is $5' \times 5'$, with north up and east to the left.

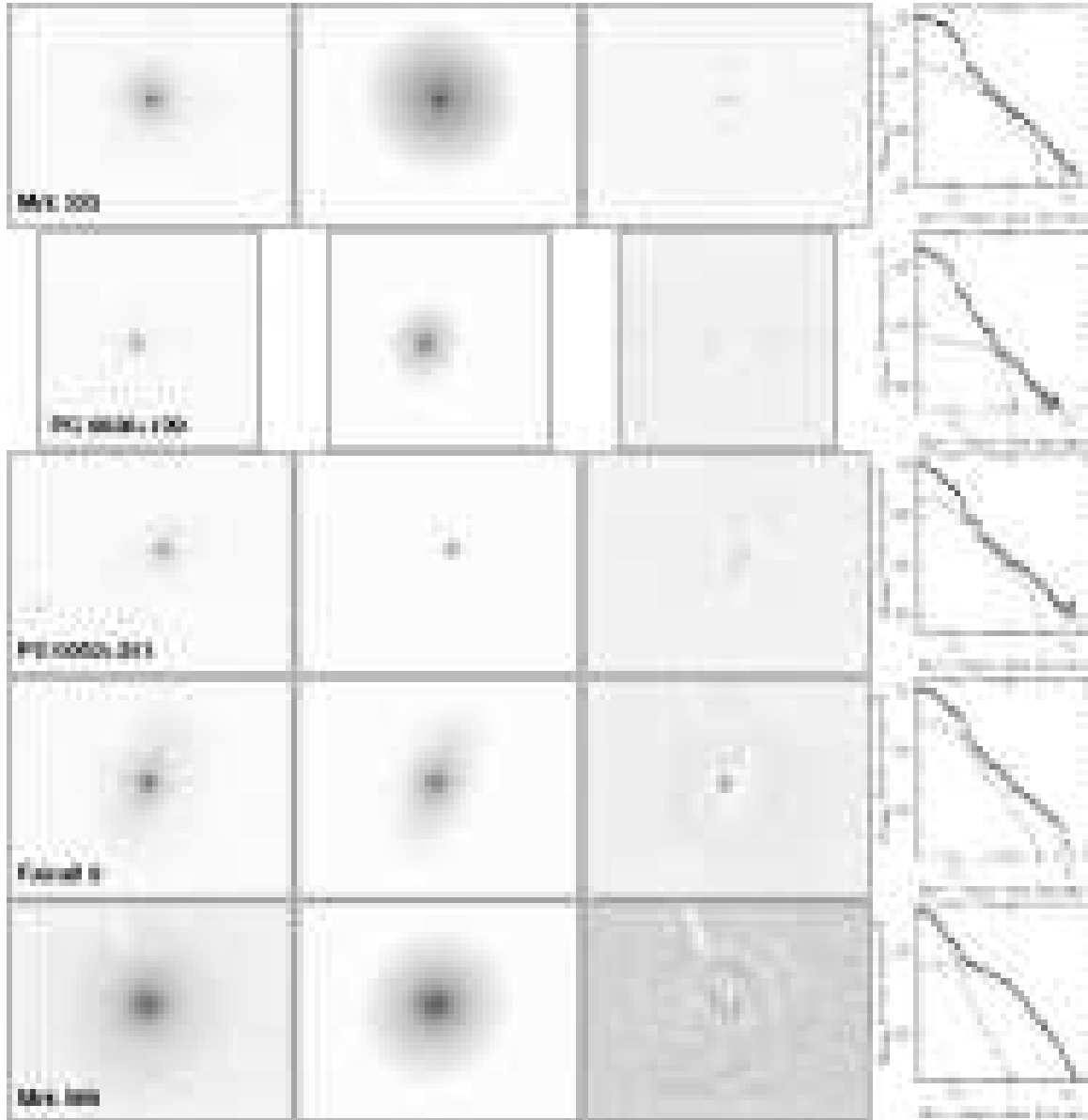
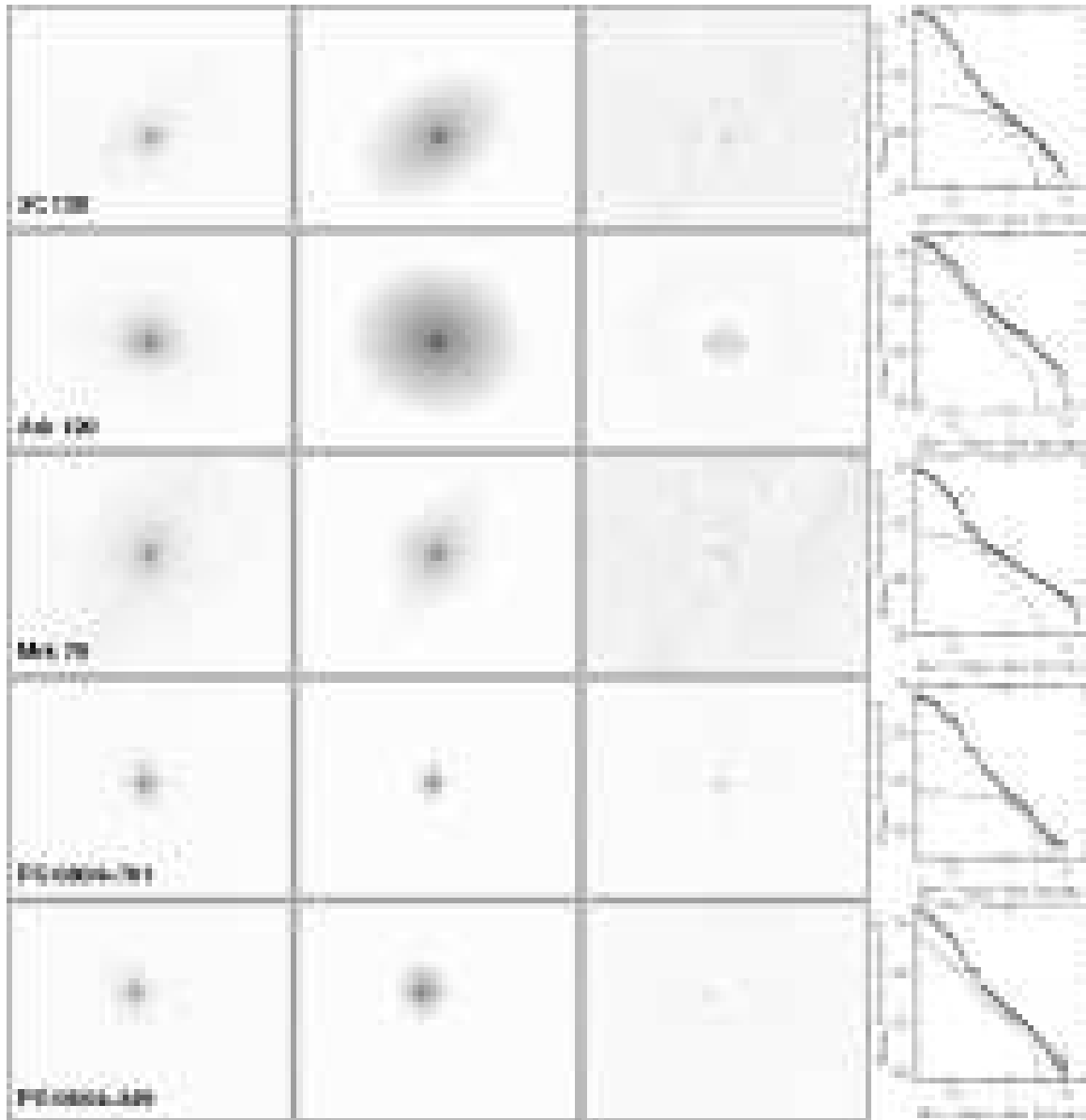


FIG. 3.— From left to right, each row shows the following: the *HST* image of an AGN and its host galaxy; the best-fit to the galaxy+AGN surface brightness profiles from Galfit; the residuals of the fit; isophotal analysis of the image and models, with the data points measured from the sky-subtracted *HST* image, the solid line from the total host-galaxy model image (which is convolved with the PSF for comparison with the observed image), and the dashed line from the PSF model for the AGN component.

FIG. 3.— *Continued.*

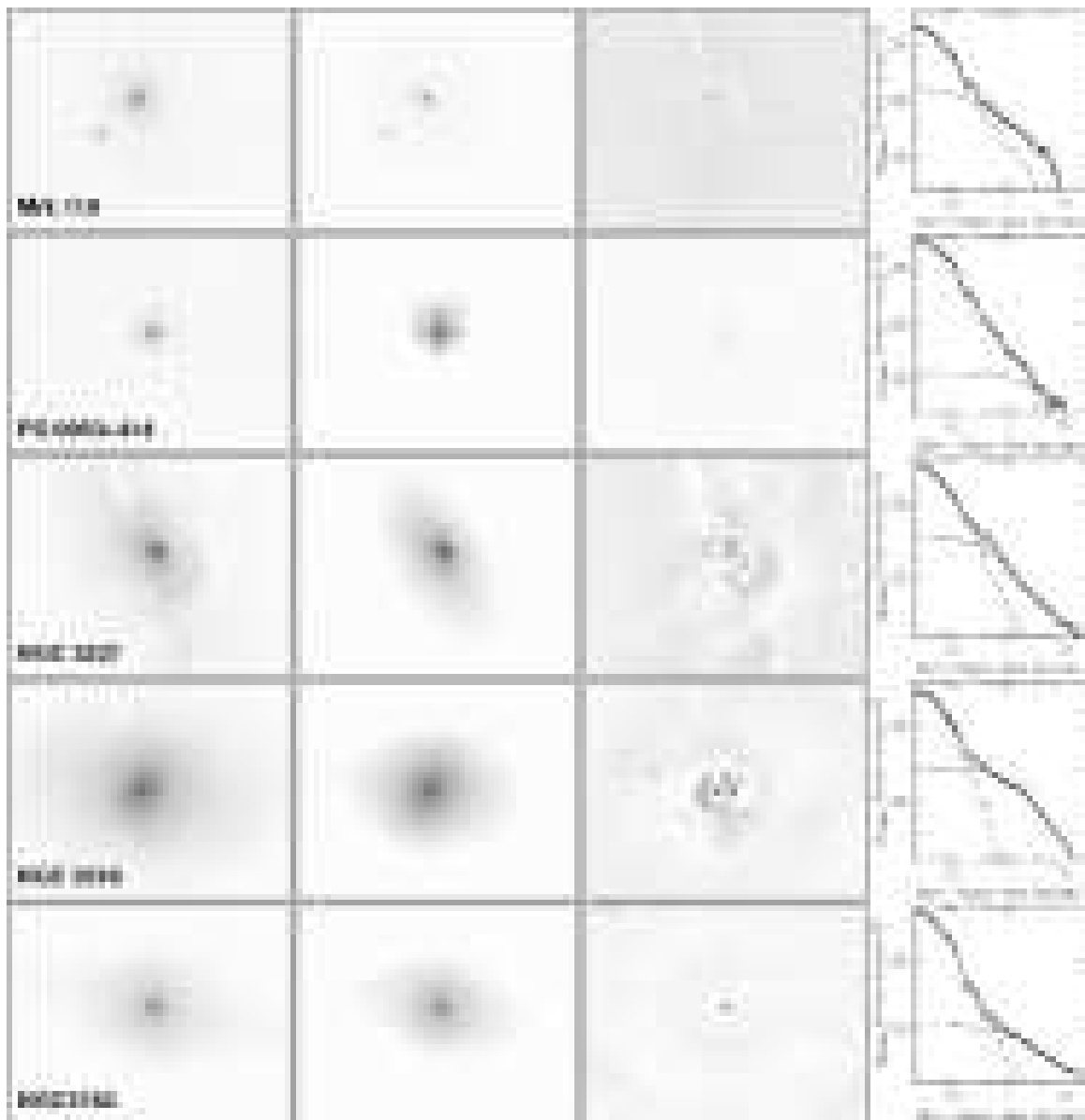
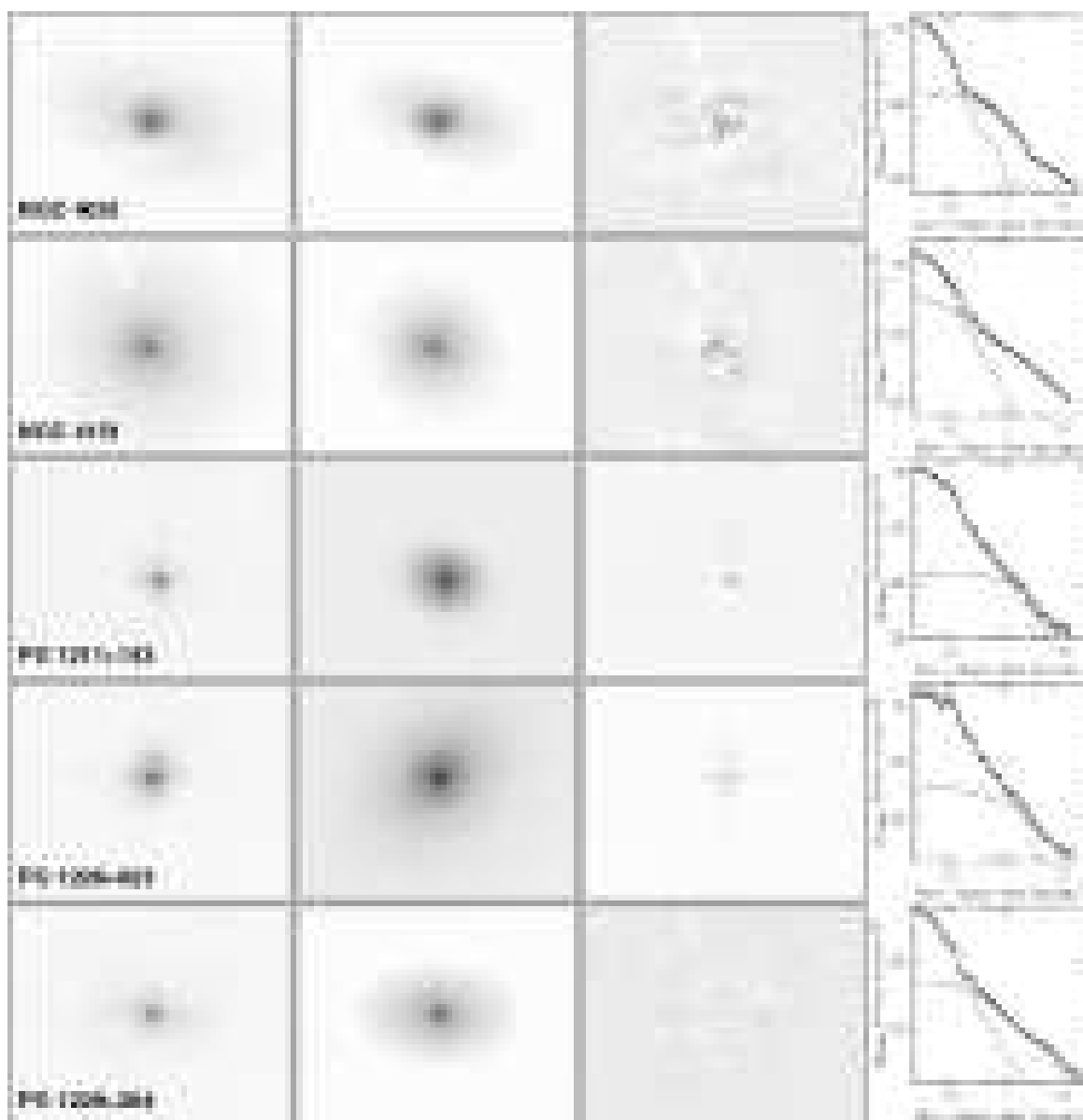


FIG. 3.— *Continued.*

FIG. 3.— *Continued.*

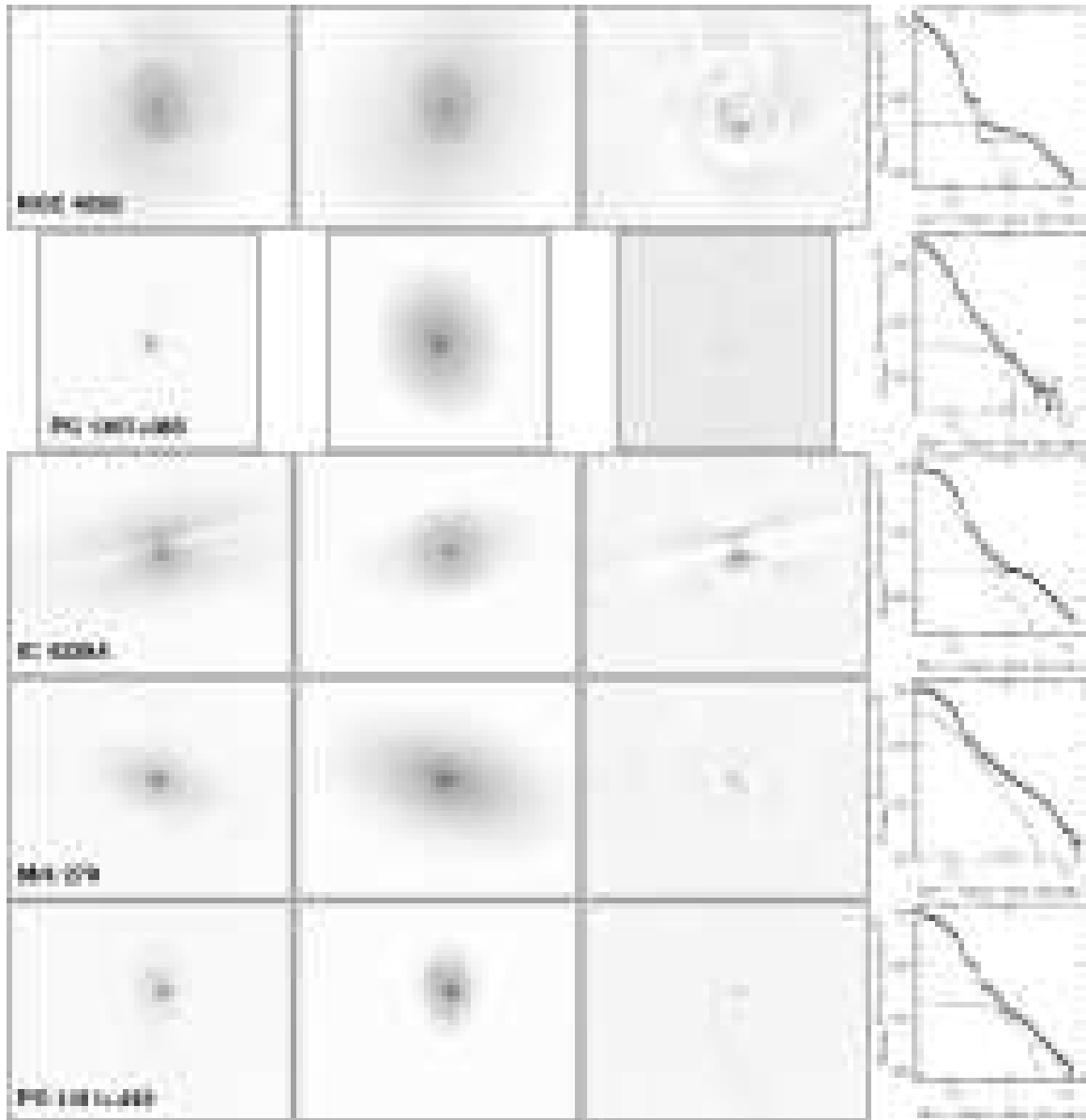
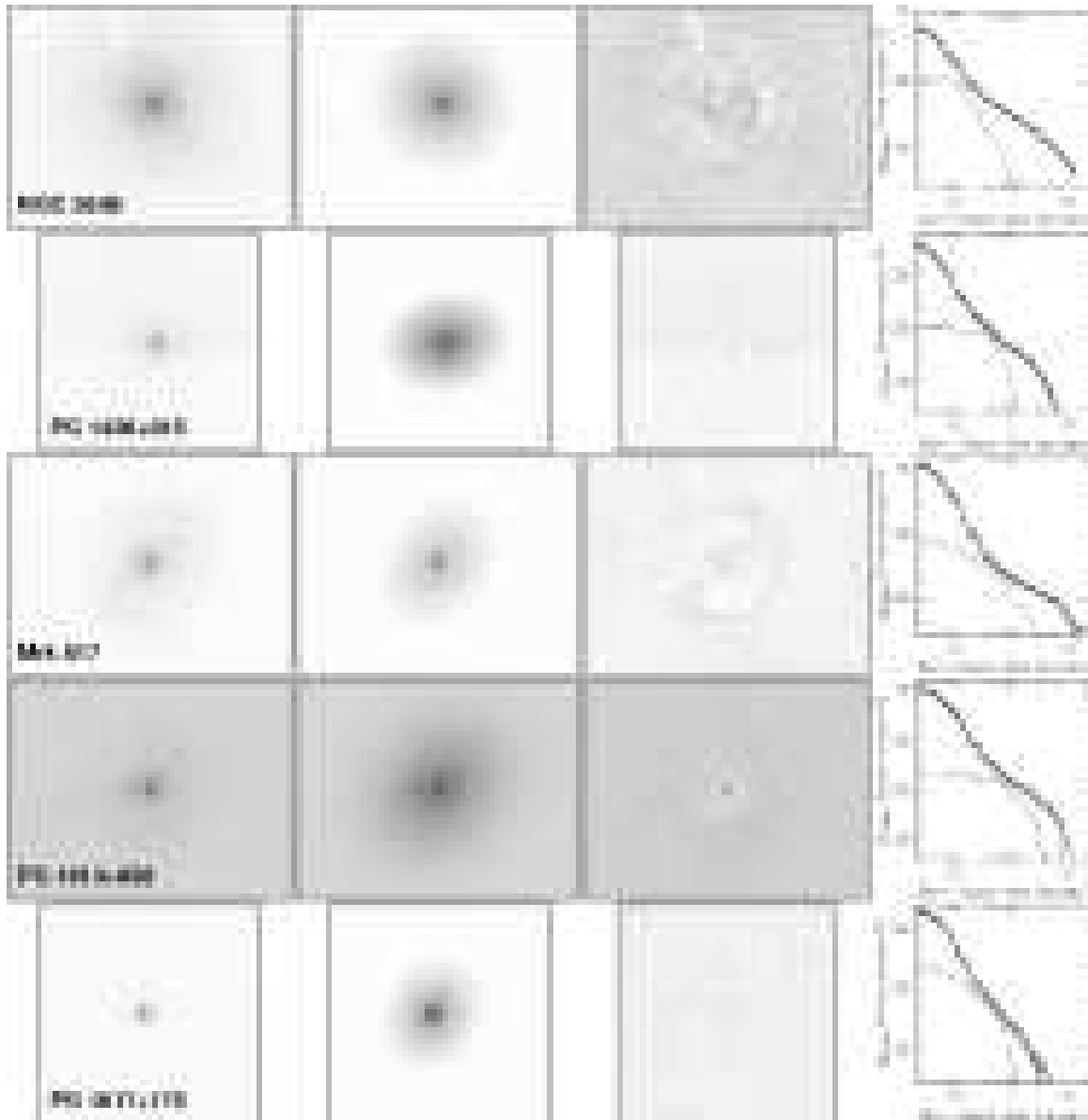


FIG. 3.— *Continued.*

FIG. 3.— *Continued.*

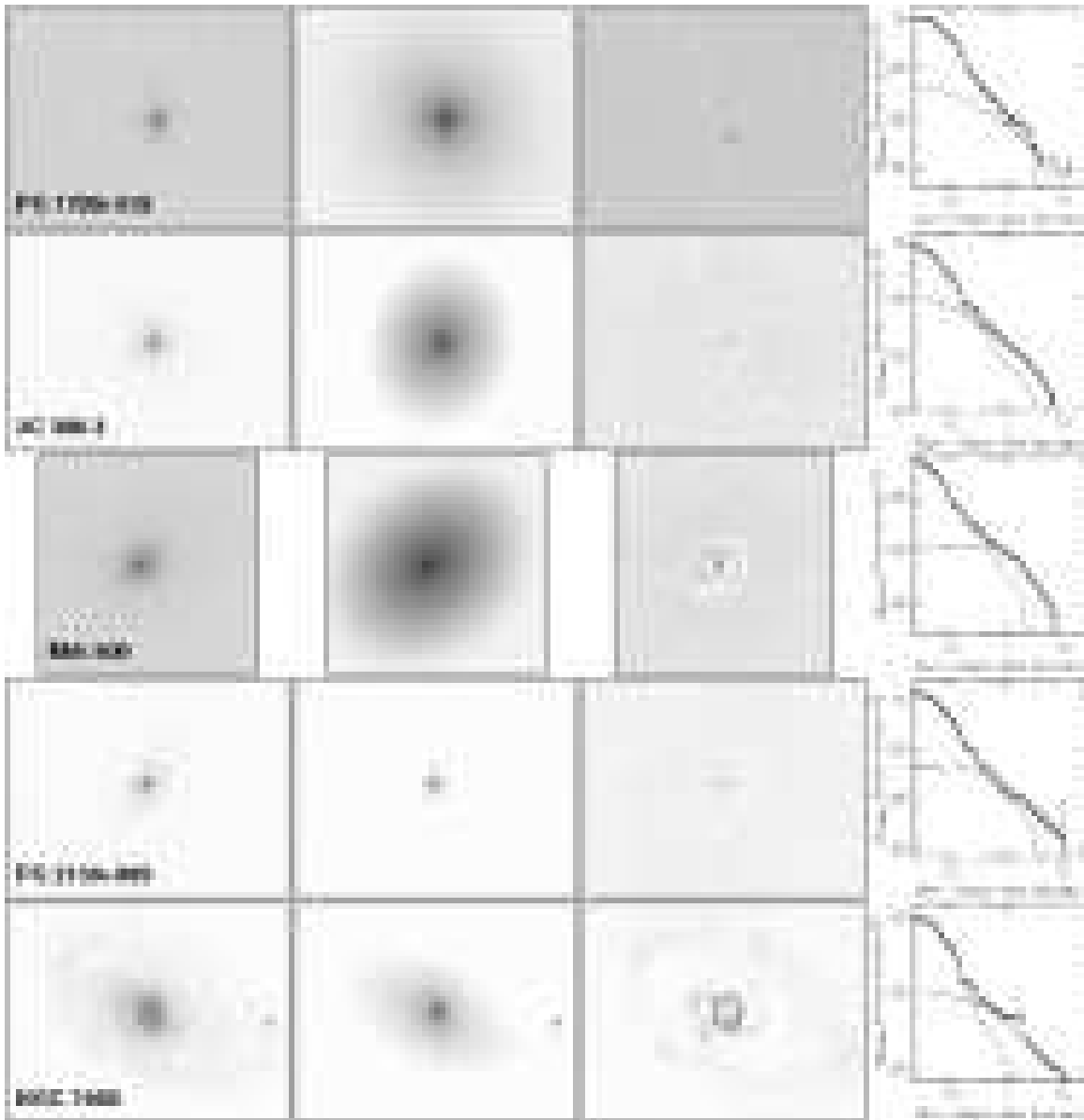


FIG. 3.— *Continued.*

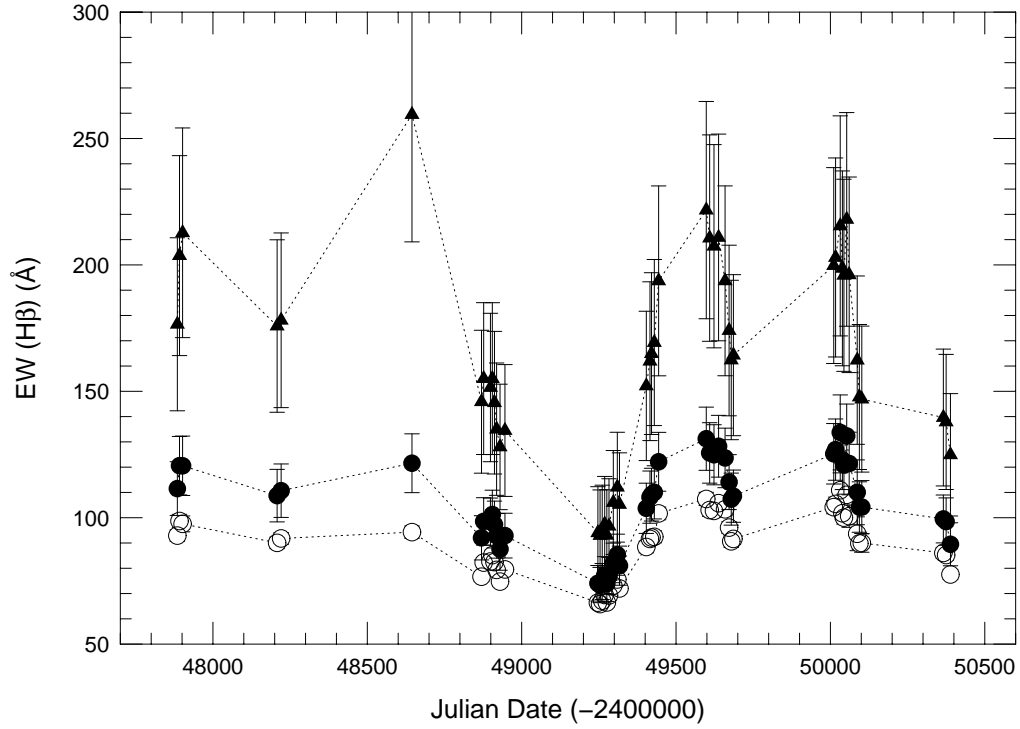


FIG. 4.— Equivalent width consistency check for 3C 120. The equivalent width of the $H\beta$ emission line is shown as a function of time for three cases: with no correction of the continuum flux density for host-galaxy contamination (open circles); with corrections for the host galaxy using the value from Bentz et al. (2006a) (triangles); and with corrections for the host galaxy using the revised value presented here in Table 7 (filled circles). The larger host-galaxy correction from Bentz et al. leads to equivalent widths that are unacceptably large and variable. The new, more conservative value for the starlight contribution corrects this problem so that the equivalent width values and variations are in keeping with expectations from photoionization physics.

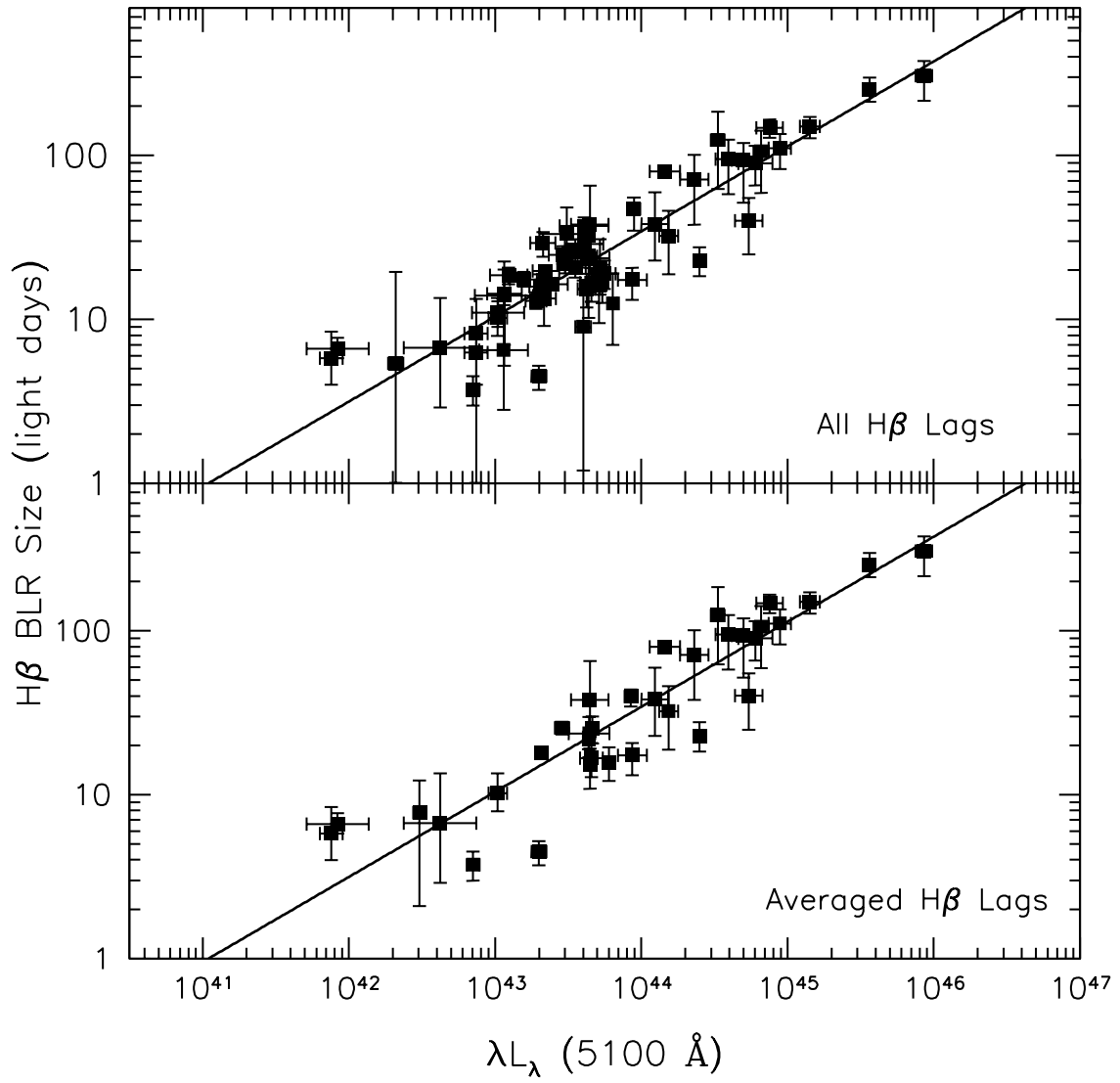


FIG. 5.— The $H\beta R_{\text{BLR}}-L$ relationship after correcting the AGN luminosities for the contribution from host-galaxy starlight. The top panel shows each separate measurement as a single data point, and the bottom panel shows the weighted mean of multiple measurements for any individual object. The solid lines are the best fit to the relationship (listed in bold face in Table 9), which has a slope of $\alpha = 0.519^{+0.063}_{-0.066}$.

TABLE 1
OBJECT LIST

Object	α_{2000} (hr min sec)	δ_{2000} ($^{\circ}$ $'$ $''$)	z	D_L^a Mpc	A_B^b (mag)	Alternate Name
Mrk 335	00 06 19.521	+20 12 10.49	0.02579	112.6	0.153	PG 0003+199
PG 0026+129	00 29 13.6	+13 16 03	0.14200	671.7	0.307	
PG 0052+251	00 54 52.1	+25 25 38	0.15500	740.0	0.205	
Fairall 9	01 23 45.780	-58 48 20.50	0.04702	208.6	0.116	
Mrk 590	02 14 33.562	-00 46 00.09	0.02639	115.3	0.161	NGC 863
3C 120	04 33 11.0955	+05 21 15.620	0.03301	145.0	1.283	Mrk 1506
Ark 120	05 16 11.421	-00 08 59.38	0.03271	141.8	0.554	Mrk 1095
Mrk 79	07 42 32.797	+49 48 34.75	0.02219	96.7	0.305	
PG 0804+761	08 10 58.600	+76 02 42.00	0.10000	460.5	0.150	
PG 0844+349	08 47 42.4	+34 45 04	0.06400	287.4	0.159	
Mrk 110	09 25 12.870	+52 17 10.52	0.03529	155.2	0.056	
PG 0953+414	09 56 52.4	+41 15 22	0.23410	1172.1	0.054	
NGC 3227	10 23 30.5790	+19 51 54.180	0.00386	23.6	0.098	
NGC 3516	11 06 47.490	+72 34 06.88	0.00884	38.1	0.183	
NGC 3783	11 39 01.72	-37 44 18.9	0.00973	42.0	0.514	
NGC 4051	12 03 09.614	+44 31 52.80	0.00234	15.2	0.056	
NGC 4151	12 10 32.579	+39 24 20.63	0.00332	14.3	0.119	
PG 1211+143	12 14 17.7	+14 03 12.6	0.08090	367.6	0.150	
PG 1226+023	12 29 06.6997	+02 03 08.598	0.15834	757.5	0.089	3C 273
PG 1229+204	12 32 03.605	+20 09 29.21	0.06301	282.8	0.117	Mrk 771 & Ton 1542
NGC 4593	12 39 39.425	-05 20 39.34	0.00900	38.8	0.106	Mrk 1330
PG 1307+085	13 09 47.0	+08 19 48.9	0.15500	739.2	0.145	
IC 4329A	13 49 19.26	-30 18 34.0	0.01605	69.6	0.255	
Mrk 279	13 53 03.447	+69 18 29.57	0.03045	133.5	0.068	
PG 1411+442	14 13 48.3	+44 00 14	0.08960	409.7	0.036	
NGC 5548	14 17 59.534	+25 08 12.44	0.01718	74.5	0.088	
PG 1426+015	14 29 06.588	+01 17 06.48	0.08647	394.4	0.137	
Mrk 817	14 36 22.068	+58 47 39.38	0.03146	137.9	0.029	PG 1434+590
PG 1613+658	16 13 57.179	+65 43 09.58	0.12900	605.6	0.114	Mrk 876
PG 1617+175	16 20 11.288	+17 24 27.70	0.11244	521.9	0.180	Mrk 877
PG 1700+518	17 01 24.800	+51 49 20.00	0.29200	1509.6	0.151	
3C 390.3	18 42 08.9899	+79 46 17.127	0.05610	250.5	0.308	
Mrk 509	20 44 09.738	-10 43 24.54	0.03440	151.2	0.248	
PG 2130+099	21 32 27.813	+10 08 19.46	0.06298	282.6	0.192	II Zw 136 & Mrk 1513
NGC 7469	23 03 15.623	+08 52 26.39	0.01632	70.8	0.297	Mrk 1514

^a Distances were calculated from the redshifts of the objects, except for NGC 3227 – where we use the distance measured by surface brightness fluctuations to NGC 3226 (Blakeslee et al. 2001), with which NGC 3227 is interacting – and NGC 4051 – where we use the average Tully-Fisher distance reported by Russell (2003).

^b Values are from Schlegel et al. (1998).

TABLE 2
HST OBSERVATION LOG

Object	Observational Setup	Date Observed (yyyy–mm–dd)	Beginning UTC (hh:mm)	Total Exposure Time (s)	Dataset
Mrk 335	ACS,HRC,F550M	2006-08-24	08:26	2040	J9MU010
PG 0026+129	WFPC2,F547M	2007-06-06	21:39	1445	U9MU520
PG 0052+251	ACS,HRC,F550M	2006-08-28	09:59	2040	J9MU030
Fairall 9	ACS,HRC,F550M	2003-08-22	00:44	1020	J8SC040
Mrk 590	ACS,HRC,F550M	2003-12-18	02:27	1020	J8SC050
3C 120	ACS,HRC,F550M	2003-12-05	05:48	1020	J8SC060
Akn 120	ACS,HRC,F550M	2006-10-30	18:36	2040	J9MU540
Mrk 79	ACS,HRC,F550M	2006-11-08	18:33	2040	J9MU050
PG 0804+761	ACS,HRC,F550M	2006-09-20	23:09	2040	J9MU060
PG 0844+349	ACS,HRC,F550M	2004-05-10	20:11	1020	J8SC100
Mrk 110	ACS,HRC,F550M	2004-05-28	17:34	1020	J8SC110
PG 0953+414	ACS,HRC,F550M	2006-10-25	18:51	2040	J9MU070
NGC 3227	ACS,HRC,F550M	2004-03-20	04:28	1020	J8SC130
NGC 3516	ACS,HRC,F550M	2005-12-19	01:03	2220	J9DQ010
NGC 3783	ACS,HRC,F550M	2003-11-15	00:11	1020	J8SC150
NGC 4051	ACS,HRC,F550M	2004-02-16	01:49	1020	J8SC160
NGC 4151	ACS,HRC,F550M	2004-03-28	14:25	1020	J8SC170
PG 1211+143	ACS,HRC,F550M	2006-11-28	02:30	2040	J9MU080
PG 1226+023	ACS,HRC,F550M	2007-01-17	12:40	2040	J9MU090
PG 1229+204	ACS,HRC,F550M	2006-11-20	02:41	2040	J9MU100
NGC 4593	ACS,HRC,F550M	2006-01-30	21:05	2220	J9DQ020
PG 1307+085	WFPC2,F547M	2007-03-21	14:36	1445	U9MU110
IC 4329A	ACS,HRC,F550M	2006-02-22	00:03	2220	J9DQ040
Mrk 279	ACS,HRC,F550M	2003-12-07	03:54	1020	J8SC240
PG 1411+442	ACS,HRC,F550M	2006-11-10	23:52	2040	J9MU120
NGC 5548	ACS,HRC,F550M	2004-04-07	01:53	1020	J8SC270
PG 1426+015	WFPC2,F547M	2007-03-20	16:18	1445	U9MU130
Mrk 817	ACS,HRC,F550M	2003-12-08	18:08	1020	J8SC290
PG 1613+658	ACS,HRC,F550M	2006-11-12	04:44	2040	J9MU140
PG 1617 175	WFPC2,F547M	2007-03-19	17:59	1445	U9MU150
PG 1700+518	ACS,HRC,F550M	2006-11-16	07:51	2040	J9MU160
3C 390.3	ACS,HRC,F550M	2004-03-31	06:56	1020	J8SC340
Mrk 509	WFPC2,F547M	2007-04-01	22:50	1445	U9MU170
PG 2130+099	ACS,HRC,F550M	2003-10-21	06:47	1020	J8SC360
NGC 7469	ACS,HRC,F550M	2006-07-09	22:00	2220	J9DQ030

TABLE 3
MDM OBSERVATION LOG

Object	Date Observed (yyyy–mm–dd)	Airmass (sec z)	Exposure Times			Seeing (″)
			<i>B</i> (s)	<i>V</i> (s)	<i>R</i> (s)	
NGC 3227	2003-02-08	1.023–1.135	1800	1680	795	1.77
NGC 3516	2003-04-25	1.317–1.392	1900	845	1500	1.85
NGC 4051	2003-02-08	1.048–1.111	1250	795	690	1.71
NGC 4151	2003-02-09	1.008–1.050	1470	1200	1220	2.07
NGC 4593	2003-02-09	1.298–1.576	1650	1860	1380	2.58
NGC 5548	2003-04-25	1.018–1.308	4000	2500	1080	1.63
NGC 7469	2003-09-26	1.087–1.106	1440	1260	1560	1.69

TABLE 4
DETAILS OF GALAXY FITS

Object	Sky (counts)	m_{stmag}^a	R_e (kpc)	n	b/a	Note
Mrk 335	10.0	14.9				PSF
		16.3	0.51	6.61	0.84	Bulge
		15.8	1.49	1.00	0.95	Disk
PG 0026+129	2.8	16.1				PSF
		17.0	0.16	2.58	0.52	Add'l PSF
		17.3	7.21	1.72	0.86	Bulge
PG 0052+251	5.7	15.6				PSF
		18.0	0.17	3.12	0.34	Bulge
		17.2	8.24	1.00	0.69	Disk
Fairall 9	7.0	18.8	3.77	5.47	0.78	Field galaxy
		15.1				PSF
		15.3	0.49	5.61	0.94	Bulge
Mrk 590	6.8	15.3	2.92	1.00	0.44	Disk
		17.9				PSF
		16.3	0.44	1.22	0.62	Inner bulge
3C 120	8.0	15.8	0.75	0.59	0.96	Bulge
		14.2	3.14	1.00	0.91	Disk
		14.9				PSF
Ark 120	12.3	18.3	0.04	3.67	0.10	Add'l PSF
		17.6	0.66	1.10	0.89	Bulge
		16.1	3.11	1.00	0.65	Disk
Mrk 79	13.7	14.7				PSF
		15.0	0.05	3.62	0.84	Bulge
		14.9	1.85	1.00	0.87	Disk
PG 0804+761	10.7	15.7				PSF
		16.1	0.85	2.79	0.67	Bulge
		16.6	1.98	1.00	0.66	Disk
PG 0844+349	6.0	14.7	8.89	0.55	0.24	Bar
		15.0				PSF
		14.7	0.08	1.22	0.73	Add'l PSF
Mrk 110	3.7	16.8	3.33	1.00	0.74	Bulge
		14.6				PSF
		16.9	0.04	2.28	0.12	Bulge
NGC 3227	14.2	16.7	2.86	1.00	0.75	Disk
		16.1				PSF
		18.2	0.25	1.35	0.85	Bulge
NGC 3516	12.0	16.5	1.73	1.00	0.93	Disk
		16.6				Star
		15.2				PSF
PG 0953+414	10.0	15.4	0.01	1.51	0.92	Add'l PSF
		14.9	0.06	1.08	0.68	Inner bulge
		12.8	1.19	2.14	0.50	Bulge
NGC 3783	12.0	13.8	4.66	1.00	0.47	Disk
		15.2				PSF
		13.4	0.38	1.24	0.77	Inner bulge
NGC 4051	8.0	13.0	1.74	0.96	0.60	Bulge
		14.4	4.53	1.00	0.52	Disk
		14.9				PSF
NGC 4151	0.2	17.7	28.82	1.39	0.55	Bulge
		14.2				PSF
		14.7	0.49	1.09	0.92	Bulge
PG 1211+143	17.0	15.0	1.95	0.33	0.29	Bar
		12.0	6.02	1.00	0.83	Disk
		14.8				PSF
PG 1226+023	6.5	15.1	0.03	1.07	0.85	Inner bulge
		15.1	0.07	0.31	0.71	Inner bulge
		12.8	0.86	1.80	0.49	Bulge
PG 1229+204	15.6	12.4	4.24	1.00	0.67	Disk
		14.5				PSF
		14.4	0.07	4.29	0.54	Inner bulge
NGC 4593	15.0	14.0	0.14	0.71	0.96	Inner bulge
		12.0	0.73	0.81	0.95	Bulge
		13.0	3.77	1.00	0.69	Disk
PG 1211+143	17.0	22.5				PSF
		14.9	0.06	0.08	0.63	Add'l PSF
		17.3	2.59	1.00	0.84	Bulge
PG 1226+023	6.5	15.4				PSF
		13.2	0.14	0.22	0.29	Add'l PSF
		15.6	11.71	2.50	0.75	Bulge
PG 1229+204	15.6	16.7				PSF
		20.2	0.23	0.82	0.69	Bar?
		17.3	0.99	1.15	0.87	Bulge
NGC 4593	15.0	15.8	7.84	1.00	0.62	Disk
		15.3				PSF
		15.1	0.52	0.09	0.71	Inner bulge

TABLE 4 — *Continued*

Object	Sky (counts)	m_{stmag}^a	R_e (kpc)	n	b/a	Note
PG 1307+085	1.3	12.3	2.83	1.94	0.68	Bulge
		13.5	9.68	1.00	0.52	Disk
		15.6				PSF
IC 4329A	15.0	18.1	0.19	0.43	0.05	Add'l PSF
		17.6	8.74	1.25	0.80	Bulge
		14.6				PSF
Mrk 279	6.0	13.8	0.01	0.31	0.87	Add'l PSF
		13.7	0.77	0.39	0.96	Inner bulge
		12.6	3.36	0.50	0.43	Bulge
PG 1411+442	9.3	15.8	8.74	1.00	0.41	Disk
		15.0				PSF
		16.2	0.05	5.94	0.65	Inner bulge
NGC 5548	0.2	16.2	0.97	1.88	0.60	Bulge
		15.2	3.14	1.00	0.54	Disk
		15.7				PSF
PG 1426+015	1.8	15.8	0.05	1.00	0.48	Add'l PSF
		16.8	5.05	1.71	0.58	Bulge
		18.8	1.87	2.23	0.64	Field galaxy
Mrk 817	4.7	16.7				PSF
		14.7	1.18	4.36	0.86	Inner bulge
		13.8	2.95	1.39	0.90	Bulge
PG 1613+658	11.0	15.5	11.51	1.00	0.85	Disk
		15.2				PSF
		16.3	4.74	1.63	0.77	Bulge
PG 1617+175	1.3	19.8	0.91	3.14	0.56	Field galaxy
		21.7	0.15	1.98	0.50	Field galaxy
		15.1				PSF
PG 1700+518	9.0	17.7	0.28	2.44	0.81	Bulge
		14.4	4.32	1.00	0.74	Disk
		15.2				PSF
3C 390.3	1.3	16.3	6.75	1.35	0.80	Bulge
		19.1	1.79	3.64	0.60	Field galaxy
		16.3				PSF
Mrk 509	4.2	17.4	0.15	0.09	0.07	Add'l PSF
		17.3	3.28	5.35	0.84	Bulge
		19.2				PSF
PG 2130+099	4.0	15.3	0.15	0.02	0.58	Add'l PSF
		16.9	0.28	0.37	0.65	Add'l PSF
		17.7	12.06	5.61	0.89	Bulge
NGC 7469	7.0	15.8				PSF
		17.0	0.77	3.86	0.74	Bulge
		16.9	2.54	1.00	0.86	Disk
Mrk 509	4.2	14.5				PSF
		15.4	0.04	0.03	0.48	Add'l PSF
		15.0	1.85	1.00	0.79	Bulge
PG 2130+099	4.0	14.8				PSF
		18.9	0.38	0.56	0.37	Bulge
		16.5	4.66	1.00	0.55	Disk
NGC 7469	7.0	15.2				PSF
		15.0	0.37	1.37	0.70	Inner bulge
		13.4	3.68	1.31	0.55	Bulge
NGC 7469	7.0	14.6	6.99	1.00	0.94	Disk
		16.2				Star

^a The magnitude of an object is computed as: $m_{stmag} = -2.5 \log \left(\frac{\text{counts}}{s} \right) + z_{pt}$, where $z_{pt} = 24.457$ for the F550M filter with ACS HRC and $z_{pt} = 21.685$ for the F547M filter with the PC chip on WFPC2.

TABLE 5
GLOBAL GALAXY PARAMETERS

Object	$\lambda L_{\lambda, \text{gal}}(5100)^{\text{a}}$ (10^{44} ergs s^{-1})	B/T		Morphological Classification	Flag ^c
		1	2 ^b		
Mrk 335	0.37	0.37		S0/a	
PG 0026+129	2.3	1.00		E1	*
PG 0052+251	4.1	0.32		Sb	
Fairall 9	2.4	0.52		SBa	*
Mrk 590	1.4	0.17	0.28	SA(s)a	
3C 120	0.73	0.21		S0	
Akn 120	2.1	0.49		Sb pec	
Mrk 79	0.73	0.19	0.87	SBb	
PG 0804+761	1.5	1.00		E3	*
PG 0844+349	1.2	0.45		Sa	*
Mrk 110	0.26	0.17		Sc	*
PG 0953+414	3.6	1.00		E4	*
NGC 3227	0.23	0.65	0.74	SAB(s) pec	
NGC 3516	0.69	0.52	0.86	(R)SB(s)	
NGC 3783	1.5	0.07	0.12	(R')SB(r)a	
NGC 4051	0.16	0.36	0.45	SAB(rs)bc	
NGC 4151	0.20	0.60	0.75	(R')SAB(rs)ab	
PG 1211+143	0.59	1.00		E2	*
PG 1226+023	11.3	1.00		E3	*
PG 1229+204	1.8	0.20	0.21	SBc	*
NGC 4593	0.91	0.71	0.76	(R)SB(rs)b	
PG 1307+085	1.8	1.00		E2	*
IC 4329A	2.4	0.70	0.96	SA0	
Mrk 279	0.95	0.21	0.43	S0	
PG 1411+442	1.2	1.00		E4	*
NGC 5548	0.98	0.60	0.87	(R')SA(s)0/a	
PG 1426+015	1.8	1.00		E2	*
Mrk 817	1.2	0.05		SBc	
PG 1613+658	4.2	1.00		E2	*
PG 1617+175	1.3	1.00		E2	*
PG 1700+518	6.7	1.00		E1	*
3C 390.3	0.87	0.48		Sa	*
Mrk 509	0.95	1.00		E2	*
PG 2130+099	0.88	0.10		(R)Sa	
NGC 7469	1.4	0.64	0.79	(R')SAB(rs)a	

^a Galaxy luminosities are determined directly from the model parameters that were fit to the *HST* images. They do not include features that were not modeled, such as the nuclear starburst ring in NGC 7469, and do not include the contributions from field galaxies or stars.

^b Bulge luminosities here include the contribution from any bar and/or inner bulge component.

^c Morphological classifications are from NED where available. Those marked with a flag are determined from the galaxy fit parameters in this work, as described in the text.

TABLE 6
GROUND-BASED MONITORING APERTURES AND OBSERVED FLUXES

Object	Reference ^a	PA (°)	Aperture (" × ")		$f((1+z)5100)$ (10^{-15} ergs s ⁻¹ cm ⁻² Å ⁻¹)
Mrk 335	1	90.0	5.0	× 7.6	7.68 ± 0.53
	1	90.0	5.0	× 7.6	8.81 ± 0.47
PG 0026+129	2	42.0	10.0	× 13.0	2.69 ± 0.40
PG 0052+251	2	153.4	10.0	× 13.0	2.07 ± 0.37
Fairall 9	3	0.0	4.0	× 9.0	5.95 ± 0.66
Mrk 590	1	90.0	5.0	× 7.6	7.89 ± 0.62
	1	90.0	5.0	× 7.6	5.33 ± 0.56
	1	90.0	5.0	× 7.6	6.37 ± 0.45
	1	90.0	5.0	× 7.6	8.43 ± 1.30
3C 120	1	90.0	5.0	× 7.6	4.30 ± 0.77
Akn 120	1	90.0	5.0	× 7.6	10.37 ± 0.46
	1	90.0	5.0	× 7.6	7.82 ± 0.83
Mrk 79	1	90.0	5.0	× 7.6	6.96 ± 0.67
	1	90.0	5.0	× 7.6	8.49 ± 0.86
	1	90.0	5.0	× 7.6	7.40 ± 0.72
PG 0804+761	2	315.6	10.0	× 13.0	5.48 ± 1.00
PG 0844+349	2	36.8	10.0	× 13.0	3.71 ± 0.38
Mrk 110	1	90.0	5.0	× 7.6	3.45 ± 0.36
	1	90.0	5.0	× 7.6	3.96 ± 0.51
	1	90.0	5.0	× 7.6	2.64 ± 0.86
PG 0953+414	2	31.7	10.0	× 13.0	1.56 ± 0.21
NGC 3227	4	25.0	1.5	× 4.0	23.46 ± 3.70
	5	90.0	5.0	× 10.0	12.70 ± 0.68
NGC 3516	6	25.0	1.5	× 2.0	7.83 ± 2.35
NGC 3783	7	0.0	5.0	× 10.0	11.38 ± 0.95
NGC 4051	8	90.0	5.0	× 7.5	13.38 ± 0.92
NGC 4151	9	90.0	5.0	× 12.75	23.8 ± 3.0
PG 1211+143	2	352.2	10.0	× 13.0	5.66 ± 0.92
PG 1226+023	2	171.2	10.0	× 13.0	21.30 ± 2.60
PG 1229+204	2	291.5	10.0	× 13.0	2.15 ± 0.23
NGC 4593	10	90.0	5.0	× 12.75	15.9 ± 0.7
PG 1307+085	2	186.5	10.0	× 13.0	1.79 ± 0.18
IC 4329A	11	90.0	5.0	× 10.0	5.79 ± 0.73
Mrk 279	12	90.0	5.0	× 7.5	6.90 ± 0.69
PG 1411+442	2	347.0	10.0	× 13.0	3.71 ± 0.32
NGC 5548	13	90.0	5.0	× 7.5	9.92 ± 1.26
	13	90.0	5.0	× 7.5	7.25 ± 1.00
	13	90.0	5.0	× 7.5	9.40 ± 0.93
	13	90.0	5.0	× 7.5	6.72 ± 1.17
	13	90.0	5.0	× 7.5	9.06 ± 0.86
	13	90.0	5.0	× 7.5	9.76 ± 1.10
	13	90.0	5.0	× 7.5	12.09 ± 1.00
	13	90.0	5.0	× 7.5	10.56 ± 1.64
	13	90.0	5.0	× 7.5	8.12 ± 0.91
	13	90.0	5.0	× 7.5	13.47 ± 1.45
	13	90.0	5.0	× 7.5	11.83 ± 1.82
	13	90.0	5.0	× 7.5	6.98 ± 1.20
	13	90.0	5.0	× 7.5	7.03 ± 0.86
	14	90.0	5.0	× 12.75	6.63 ± 0.36
PG 1426+015	2	341.4	10.0	× 13.0	4.62 ± 0.71
Mrk 817	1	90.0	5.0	× 7.6	6.10 ± 0.83
	1	90.0	5.0	× 7.6	5.00 ± 0.49
	1	90.0	5.0	× 7.6	5.01 ± 0.27
PG 1613+658	2	164.2	10.0	× 13.0	3.49 ± 0.43
PG 1617+175	2	253.0	10.0	× 13.0	1.44 ± 0.25
PG 1700+518	2	183.5	10.0	× 13.0	2.20 ± 0.15
3C 390.3	15	90.0	5.0	× 7.5	1.73 ± 0.28
Mrk 509	1	90.0	5.0	× 7.6	10.92 ± 1.99
PG 2130+099	16	0.0	3.0	× 6.97	4.63 ± 0.23
NGC 7469	17	90.0	5.0	× 7.5	13.57 ± 0.61

REFERENCES. — 1. Peterson et al. (1998), 2. Kaspi et al. (2000), 3. Santos-Lleó et al. (1997), 4. Salamanca et al. (1994), 5. Winge et al. (1995), 6. Wanders et al. (1993), 7. Stirpe et al. (1994), 8. Peterson et al. (2000), 9. Bentz et al. (2006b), 10. Denney et al. (2006), 11. Winge et al. (1996), 12. Santos-Lleó et al. (2001), 13. Peterson et al. (2002) and references therein, 14. Bentz et al. (2007), 15. Dietrich et al. (1998), 16. Grier et al. (2008), 17. Collier et al. (1998).

NOTE. — Here, and throughout, observed galaxy fluxes are tabulated at rest-frame 5100 Å.

^a References refer to reverberation-mapping campaigns in optical wavelengths.

TABLE 7
HOST-GALAXY FLUXES AND LUMINOSITIES

Object	$f_{\text{gal}}(HST)$ (10^{-15} ergs s^{-1} cm^{-2} \AA^{-1})	$\frac{f_{\text{gal}}(HST)}{f_{\text{gal}}((1+z)5100)}$	$f_{\text{gal}}((1+z)5100)$ (10^{-15} ergs s^{-1} cm^{-2} \AA^{-1})	$\lambda L_{\lambda, \text{gal}}(5100)^a$ (10^{44} ergs s^{-1})
Mrk 335	1.88	0.85	1.60 ± 0.15	0.142 ± 0.013
PG 0026+129	0.381	1.00	0.379 ± 0.035	1.46 ± 0.13
PG 0052+251	0.713	0.98	0.699 ± 0.064	3.08 ± 0.28
Fairall 9	3.47	0.88	3.07 ± 0.28	0.927 ± 0.085
Mrk 590	4.81	0.85	4.10 ± 0.38	0.384 ± 0.035
3C 120	0.783	0.82	0.641 ± 0.059	0.217 ± 0.020
Akn 120	6.70	0.85	5.68 ± 0.52	1.079 ± 0.099
Mrk 79	1.74	0.84	1.46 ± 0.13	0.106 ± 0.010
PG 0804+761	0.703	0.97	0.683 ± 0.063	1.076 ± 0.099
PG 0844+349	1.24	0.92	1.14 ± 0.11	0.684 ± 0.063
Mrk 110	0.786	0.88	0.688 ± 0.063	0.109 ± 0.010
PG 0953+414	0.208	1.11	0.231 ± 0.021	2.47 ± 0.23
NGC 3227 ^b	4.12	0.82	3.37 ± 0.31	0.0124 ± 0.0011
	8.57	0.82	7.01 ± 0.65	0.0258 ± 0.0024
NGC 3516	4.55	0.82	3.73 ± 0.34	0.0382 ± 0.0035
NGC 3783	6.06	0.80	4.86 ± 0.45	0.0776 ± 0.0071
NGC 4051	10.1	0.82	8.28 ± 0.76	0.0123 ± 0.0011
NGC 4151	21.6	0.82	17.6 ± 1.6	0.0240 ± 0.0022
PG 1211+143	0.633	0.95	0.598 ± 0.055	0.592 ± 0.054
PG 1226+023	1.37	0.98	1.34 ± 0.12	5.741 ± 0.529
PG 1229+204	1.48	0.92	1.36 ± 0.13	0.766 ± 0.071
NGC 4593	10.7	0.82	8.85 ± 0.82	0.0889 ± 0.0082
PG 1307+085	0.232	1.00	0.233 ± 0.021	0.986 ± 0.091
IC 4329A	4.43	0.83	3.67 ± 0.34	0.133 ± 0.012
Mrk 279	3.49	0.87	3.02 ± 0.28	0.355 ± 0.033
PG 1411+442	0.826	0.96	0.791 ± 0.073	0.904 ± 0.083
NGC 5548 ^b	4.63	0.84	3.88 ± 0.36	0.143 ± 0.013
	5.51	0.84	4.61 ± 0.43	0.169 ± 0.016
PG 1426+015	1.19	0.96	1.14 ± 0.11	1.29 ± 0.12
Mrk 817	1.77	0.87	1.54 ± 0.14	0.188 ± 0.017
PG 1613+658	1.52	0.98	1.50 ± 0.14	4.08 ± 0.38
PG 1617+175	0.341	0.99	0.336 ± 0.031	0.701 ± 0.065
PG 1700+518	0.246	1.41	0.347 ± 0.032	6.79 ± 0.63
3C 390.3	0.945	0.90	0.853 ± 0.079	0.430 ± 0.040
Mrk 509	2.74	0.92	2.52 ± 0.23	0.435 ± 0.040
PG 2130+099	0.440	0.92	0.405 ± 0.037	0.240 ± 0.022
NGC 7469	10.2	0.83	8.43 ± 0.78	0.327 ± 0.030

^a The galaxy luminosities presented here are measured through the ground-based monitoring aperture directly from the PSF-subtracted *HST* images. Any field galaxies or stars, or additional unmodeled galaxy structures, that are included in the original ground-based spectroscopic aperture contribute to this luminosity.

^b The two different entries for NGC 3227 and NGC 5548 correspond to the two different monitoring apertures that were employed during the spectroscopic monitoring programs for these objects. They are listed in the same order as in Table 6.

TABLE 8
REST-FRAME TIME LAGS AND STARLIGHT CORRECTED LUMINOSITIES

Object	H β Time Lag (days)	$f_{\text{AGN}} ((1+z) 5100 \text{ \AA})$ ($10^{-15} \text{ ergs s}^{-1} \text{ cm}^{-2} \text{ \AA}^{-1}$)	$\lambda L_{\lambda, \text{AGN}} (5100 \text{ \AA})$ ($10^{44} \text{ ergs s}^{-1}$)	
Mrk 335	16.8 ^{+4.8} _{-4.2}	6.09 ± 0.53	0.541 ± 0.047	
	12.5 ^{+6.6} _{-5.5}	7.21 ± 0.47	0.640 ± 0.041	
	15.7^{+3.4}_{-4.0}	6.72 ± 0.35	0.603 ± 0.031	
PG 0026+129	111.0 ^{+24.1} _{-23.2}	2.31 ± 0.40	8.9 ± 1.6	
PG 0052+251	89.8 ^{+24.1} _{-24.1}	1.37 ± 0.37	6.0 ± 1.6	
Fairall 9	17.4 ^{+3.2} _{-4.3}	2.88 ± 0.66	0.87 ± 0.20	
Mrk 590	20.7 ^{+3.5} _{-4.3}	3.80 ± 0.62	0.355 ± 0.058	
	14.0 ^{+8.5} _{-8.8}	1.23 ± 0.56	0.115 ± 0.053	
	29.2 ^{+4.9} _{-5.0}	2.27 ± 0.45	0.212 ± 0.043	
	28.8 ^{+3.6} _{-4.2}	4.3 ± 1.3	0.41 ± 0.12	
	25.6^{+2.0}_{-2.3}	2.44 ± 0.30	0.287 ± 0.032	
3C 120	38.1 ^{+21.3} _{-15.3}	3.66 ± 0.77	1.24 ± 0.26	
Ark 120	47.1 ^{+8.3} _{-12.4}	4.69 ± 0.46	0.889 ± 0.088	
	37.1 ^{+4.8} _{-5.4}	2.14 ± 0.83	0.41 ± 0.16	
	39.7^{+3.9}_{-5.2}	4.09 ± 0.40	0.847 ± 0.081	
Mrk 79	9.0 ^{+8.3} _{-7.8}	5.50 ± 0.67	0.401 ± 0.049	
	16.1 ^{+6.6} _{-6.4}	7.03 ± 0.86	0.513 ± 0.063	
	16.0 ^{+6.4} _{-5.8}	5.94 ± 0.72	0.435 ± 0.053	
	15.2^{+3.4}_{-5.1}	6.03 ± 0.43	0.447 ± 0.031	
PG 0804+761	146.9 ^{+18.8} _{-18.9}	4.8 ± 1.0	7.6 ± 1.6	
PG 0844+349 ^a	32.3 ^{+13.4} _{-13.4}	2.57 ± 0.38	1.54 ± 0.23	
Mrk 110	24.3 ^{+5.5} _{-8.3}	2.77 ± 0.36	0.439 ± 0.058	
	20.4 ^{+10.5} _{-6.3}	3.28 ± 0.51	0.520 ± 0.080	
	33.3 ^{+4.9} _{-10.0}	1.95 ± 0.86	0.31 ± 0.14	
	25.5^{+4.2}_{-5.6}	2.83 ± 0.28	0.461 ± 0.045	
PG 0953+414	150.1 ^{+21.6} _{-22.6}	1.33 ± 0.21	14.2 ± 2.2	
NGC 3227	8.2 ^{+5.1} _{-8.4}	20.1 ± 3.7	0.074 ± 0.014	
	5.4 ^{+14.1} _{-8.4}	5.70 ± 0.68	0.0209 ± 0.0025	
	7.8^{+10.2}_{-10.2}	6.17 ± 0.67	0.0304 ± 0.0031	
NGC 3516	6.7 ^{+6.8} _{-3.8}	4.1 ± 2.3	0.042 ± 0.024	
NGC 3783	10.2 ^{+3.3} _{-2.3}	6.52 ± 0.95	0.104 ± 0.015	
NGC 4051	5.8 ^{+2.6} _{-1.8}	5.10 ± 0.92	0.0076 ± 0.0014	
NGC 4151	6.6 ^{+1.1} _{-1.1}	6.2 ± 3.0	0.0084 ± 0.0041	
PG 1211+143	93.8 ^{+25.6} _{-42.1}	5.06 ± 0.92	5.00 ± 0.91	
PG 1226+032	306.8 ^{+68.5} _{-90.9}	20.0 ± 2.6	86 ± 11	
PG 1229+204	37.8 ^{+27.6} _{-15.3}	0.79 ± 0.23	0.45 ± 0.13	
NGC 4593	3.7 ^{+0.3} _{-0.8}	7.05 ± 0.70	0.0708 ± 0.0070	
PG 1307+085	105.6 ^{+36.0} _{-46.6}	1.56 ± 0.18	6.59 ± 0.77	
IC 4329A ^b	1.5 ^{+2.7} _{-1.8}	2.12 ± 0.73	0.077 ± 0.026	
Mrk 279	16.7 ^{+3.8} _{-3.9}	3.88 ± 0.69	0.456 ± 0.082	
PG 1411+442	124.3 ^{+61.0} _{-61.7}	2.92 ± 0.32	3.34 ± 0.36	
NGC 5548	19.7 ^{+1.5} _{-1.5}	6.0 ± 1.3	0.222 ± 0.047	
	18.6 ^{+1.1} _{-2.3}	3.4 ± 1.0	0.124 ± 0.037	
	15.9 ^{+2.9} _{-2.9}	5.52 ± 0.93	0.203 ± 0.034	
	11.0 ^{+1.9} _{-2.0}	2.8 ± 1.2	0.105 ± 0.043	
	13.0 ^{+1.6} _{-1.4}	5.19 ± 0.86	0.191 ± 0.032	
	13.4 ^{+3.8} _{-4.2}	5.9 ± 1.1	0.216 ± 0.040	
	21.7 ^{+2.6} _{-2.6}	8.2 ± 1.0	0.302 ± 0.037	
	16.4 ^{+1.2} _{-1.1}	6.7 ± 1.6	0.246 ± 0.060	
	17.5 ^{+2.0} _{-1.6}	4.25 ± 0.91	0.156 ± 0.033	
	26.5 ^{+4.3} _{-2.2}	9.6 ± 1.5	0.352 ± 0.054	
	24.8 ^{+3.2} _{-3.0}	8.0 ± 1.8	0.292 ± 0.067	
	6.5 ^{+3.7} _{-3.7}	3.1 ± 1.2	0.114 ± 0.044	
	14.3 ^{+5.9} _{-7.3}	3.16 ± 0.86	0.116 ± 0.032	
	6.3 ^{+2.6} _{-2.3}	2.02 ± 0.36	0.074 ± 0.013	
	18.0^{+0.6}_{-0.6}	3.84 ± 0.23	0.205 ± 0.011	
	PG 1426+015	95.0 ^{+29.9} _{-37.1}	3.48 ± 0.71	3.94 ± 0.81
	Mrk 817	19.0 ^{+3.7} _{-3.7}	4.56 ± 0.83	0.56 ± 0.10
		15.3 ^{+3.7} _{-3.5}	3.46 ± 0.49	0.423 ± 0.060
		33.6 ^{+6.5} _{-7.6}	3.47 ± 0.27	0.424 ± 0.032
		21.8^{+3.0}_{-3.0}	3.54 ± 0.23	0.438 ± 0.028
PG 1613+658	40.1 ^{+15.0} _{-15.2}	1.99 ± 0.43	5.4 ± 1.2	
PG 1617+175	71.5 ^{+29.6} _{-33.7}	1.10 ± 0.25	2.30 ± 0.51	

TABLE 8 — *Continued*

Object	H β Time Lag (days)	$f_{\text{AGN}} ((1+z) 5100 \text{ \AA})$ ($10^{-15} \text{ ergs s}^{-1} \text{ cm}^{-2} \text{ \AA}^{-1}$)	$\lambda L_{\lambda, \text{AGN}} (5100 \text{ \AA})$ ($10^{44} \text{ ergs s}^{-1}$)
PG 1700+518	251.8 ^{+45.9} _{-38.8}	1.85 ± 0.15	36.3 ± 2.9
3C 390.3	23.6 ^{+6.8} _{-6.7}	0.88 ± 0.28	0.44 ± 0.14
Mrk 509	79.6 ^{+6.1} _{-5.4}	8.4 ± 2.0	1.45 ± 0.34
PG 2130+099	22.9 ^{+4.7} _{-4.6}	4.22 ± 0.23	2.51 ± 0.14
NGC 7469	4.5 ^{+0.7} _{-0.8}	5.14 ± 0.61	0.200 ± 0.023

NOTE. — Numbers in boldface are the weighted averages of all the measurements for that particular object. Fluxes are as observed. Time lags and luminosities are listed in the rest-frame of the object with weighted averages calculated in log space.

^a The H β lag measurement for this object was deemed unreliable by Peterson et al. (2004). In its place, we give the most reliably measured lag, which is for H α .

^b Because of the extremely poor lag measurement (which is consistent with zero) and the poor flux calibration for this object, we do not include it in the fit to the $R_{\text{BLR}}-L$ relationship.

TABLE 9
H β $R_{\text{BLR}}-L$ FITS

Note	N	K	α	Scatter ^a
FITEXY				
All	59	-21.0 ± 1.8	0.511 ± 0.041	34.0
Avg	34	-22.1 ± 2.3	0.535 ± 0.051	40.0
MC	34	-22.3 ± 2.2	$0.540^{+0.054}_{-0.055}$	$40.3^{+1.1}_{-0.9}$
BCES				
All	59	-20.4 ± 1.8	0.499 ± 0.042	...
Avg	34	-21.5 ± 2.1	0.524 ± 0.046	...
MC ^b	34	$-21.3^{+2.9}_{-2.8}$	$0.519^{+0.063}_{-0.066}$...
GaussFit				
All	59	-21.7 ± 1.5	0.529 ± 0.033	...
Avg	34	-21.8 ± 1.9	0.531 ± 0.042	...
MC	34	-22.9 ± 2.2	$0.554^{+0.049}_{-0.050}$...

NOTE. — *All*: Each individual measurement is treated separately. *Avg*: Multiple measurements for a single source are combined into a weighted average. *MC*: Monte Carlo techniques are used to randomly sample the multiple measurements for a single source, producing one pair of R_{BLR} and L measurements per object. The values and uncertainties presented for the fit using this method describe the median and 68% confidence intervals for the distributions of slopes and intercepts built up over multiple realizations. As described in the text, IC 4329A was not included in any of the fits listed here.

^a The scatter listed here is the percentage of the measurement value of R_{BLR} that is added in quadrature to the error value so as to obtain a reduced χ^2 of 1.0.

^b This fit, which properly treats multiple measurements of individual objects and accounts for intrinsic scatter in the data set, should be taken as our current best estimate for the form of the $R_{\text{BLR}}-L$ relationship.